CHALMERS
UNIVERSITY OF TECHNOLOGY

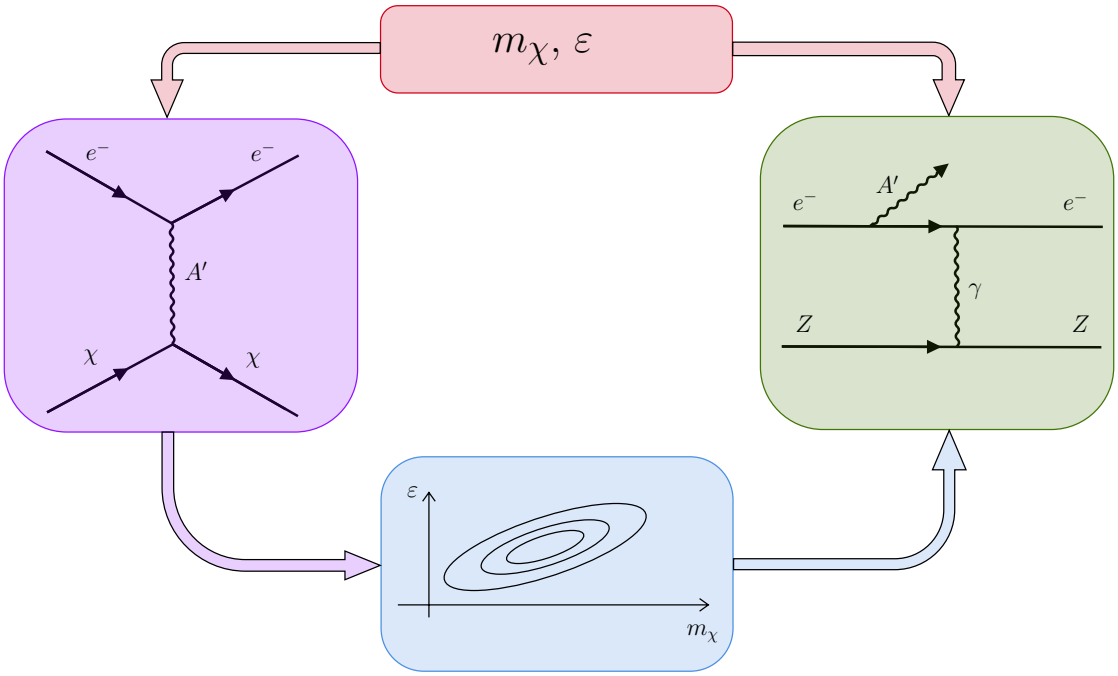

Validating the Dark Matter Origin of a LDMX Signal with Direct Detection Experiments

Master's thesis in Physics

ANDREAS LUND

DEPARTMENT OF PHYSICS

CHALMERS UNIVERSITY OF TECHNOLOGY
Gothenburg, Sweden 2024
www.chalmers.se

Master thesis 2024

Validating the Dark Matter Origin of a LDMX Signal with Direct Detection Experiments

Andreas Lund

CHALMERS
UNIVERSITY OF TECHNOLOGY

Department of Physics
Divison of Subatomic, High Energy and Plasma Physics
Chalmers University of Technology
Gothenburg, Sweden 2024

Validating the dark matter origin of a LDMX signal with direct detection experiments
Andreas Lund

Supervisor: Riccardo Catena, Department of Physics
Examinator: Riccardo Catena, Department of Physics

Master's thesis 2024
Department of Physics
Division of Subatomic, High energy and Plasma Physics
Chalmers University of Technology
SE-412 96 Gothenburg
Telephone +46 31 772 1000

Cover: Schematic illustration of the methodology used for validation in this project. The dark matter model parameters m_χ, ε (red) are used as input to simulate a direct detection electron scattering process (purple) and a LDMX dark bremsstrahlung process (green). The parameters are estimated from the direct detection process as a posterior distribution (blue), which also is input to the LDMX dark bremsstrahlung process.

Typeset in LaTeX
Gothenburg, Sweden 2024

Validating the dark matter origin of a LDMX signal with direct detection experiments
Andreas Lund
Department of Physics
Chalmers University of Technology

Abstract

The search for a particle candidate explaining the origin of dark matter is one of the central goals in modern astro-particle physics. Many experiments based on different measurement strategies are being built in an effort to detect such a candidate. In the event that a dark matter signal is seen, it is crucial to verify the signal with other experiments. In this thesis we explore the possibility of using a direct detection experiment to validate a hypothetical dark matter signal seen at the Light Dark Matter eXperiment (LDMX). We consider a representative light dark matter model with masses ranging between $\sim 1 - 1000\,\mathrm{MeV}$, which are assumed to be mediated by a massive dark photon. Hypothetical dark matter signals are simulated, both for an LDMX-type experiment and for a semiconductor based direct detection experiment. These signals are generated for varying values of the "true" dark matter mass $m_{\chi,\mathrm{true}}$ and dark photon kinetic mixing $\varepsilon_{\mathrm{true}}$ parameters, which are chosen under thermal relic abundance constraints. Validation is achieved by using the MultiNest Monte Carlo algorithm to estimate the marginal posterior of the m_χ and ε parameters given the hypothetical direct detection signal. The parameter estimate is input into the LDMX-type simulation software and compared with that of the hypothetical LDMX result. The chi-square hypothesis test is used to conclude whether the two distributions are consistent with a single distribution function. A conclusion is drawn regarding the amount of exposure required for a direct detection experiment to validate a hypothetical LDMX signal for some choices of $m_{\chi,\mathrm{true}}$. For instance, when $m_{\chi,\mathrm{true}} = 10\,\mathrm{MeV}$ the threshold exposure for validation was determined to be $0.05\,\mathrm{kg\text{-}year}$.

Keywords: dark matter, light dark matter, LDMX, direct detection, exclusion limit, experiment validation, Bayesian inference, Madgraph, DarkELF, MultiNest

Acknowledgements

First and foremost I would like to extend my deepest gratitude towards my supervisor Riccardo Catena. You have provided excellent guidance, discussion and support throughout this interesting project. Next up, I want to thank Taylor Gray for all the help and insightful discussions on various topics. I also greatly appreciate the weekly online meetings with the experimental LDMX group at Lund University. Lastly, I want to express a warm and heartfelt thank you towards my friends and family for supporting me through this hectic time in my life.

Andreas Lund, Gothenburg, June 2024

Contents

List of Acronyms

Below is the list of acronyms that have been used throughout this thesis listed in alphabetical order:

CMB	Cosmic Microwave Background
DD	Direct Detection
DM	Dark Matter
ELF	Energy Loss Function
LDM	Light Dark Matter
LDMX	Light Dark Matter eXperiment
MC	Monte Carlo
MCMC	Markov Chain Monte Carlo
PDF	Probability Density Function

List of Figures

List of Tables

1

Introduction

Since the dawn of human inquiry, we have pondered the very nature of existence. What are the underlying structures and laws of nature that govern our world? Perhaps the greatest achievement of modern science on the subatomic level is the Standard Model of particle physics (SM), which is the best experimentally verified theory for what constitutes the smallest building blocks of the Universe. As recently as 2012, one of the final missing pieces of the SM, the Higgs boson, was discovered at the Large Hadron Collider (LHC) at CERN [1]. Every particle of the standard model is categorized and shown in figure 1.1.

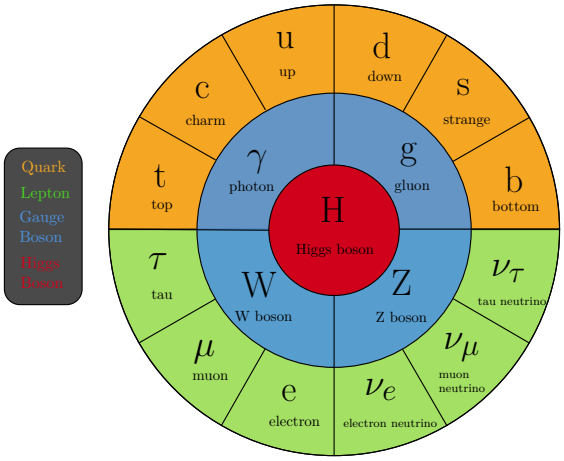

Figure 1.1: Categorization of all the particles in the Standard Model of particle physics. From these subatomic particles all ordinary matter and forces, except gravity, can be explained. We work under the conjecture that DM consists of particles beyond the SM, and look for interactions between DM and SM particles.

The accuracy with which we can describe the subatomic world with this theory cannot be overstated, but that is not to say that it is perfect or complete. For one thing, the Standard Model fails completely to describe gravity, which instead is accurately predicted by Einstein's theory of general relativity. The mismatch between these two theories is partly because gravity is immeasurably weak on subatomic scales and partly because the classical theory of general relativity fails to reconcile with the theory of quantum mechanics, which lies as bedrock to the Standard Model. Furthermore, the persistence of experimental and theoretical anomalies, such as the hierarchy problem or the strong CP problem, motivates a search beyond the standard model [2]. It is natural to conjecture

that the Standard Model is the low-energy limit of a more fundamental theory[1] and so we expect the existence of other types of particles that have not yet been discovered [2]. One prominent experimental anomaly that reinforces this conjecture is the unexplained phenomenon of so-called Dark Matter (DM).

The mystery of dark matter has emerged as one of the greatest unsolved problems in physics today. Dark matter is hypothesised as a type of matter that has only been seen to interact with SM matter through gravitation, and so is practically invisible to all other forces. Despite this, there is ample evidence for DM based on extensive astronomical observations. The cosmological Λ-CDM model has been used with data collected during the Planck mission to predict that dark matter makes up 5 times more of the energy-matter density of the universe compared to regular baryonic matter [4]. The largely unknown nature of DM phenomenology has given rise to a plethora of theories aiming to explain the nature of this elusive type of matter. The hope is that the next particle(s) we discover beyond the standard model will explain the dark matter anomaly.

An extensive effort is being put into experiments that aim to detect some faint non-gravitational interaction that could be attributed to dark matter. One promising experiment type are particle collider experiments built upon the beam dump setup. In these experiments, high energy accelerated particles, usually electrons or muons, are shot at a fixed target in the hopes of detecting DM production events. One such experiment that is in its construction phase is the Light Dark Matter eXperiment (LDMX) being built in the SLAC laboratory at Stanford, which has been designed by collaborators at Lund University [5]. As the name suggests, the experiment aims to primarily probe for light dark matter candidates, which encompasses DM masses in the range $1\,\mathrm{MeV} \lesssim m_\chi \lesssim 1\,\mathrm{GeV}$ [2] similarly to that of the proton and electron [6]. Up until recently, this region of dark matter candidates has mostly been overlooked experimentally.

Experiments other than LDMX are actively being pursued with distinct measurement strategies. Whereas LDMX is aiming to produce DM in a laboratory, direct detection experiments look for interactions between a material and the local DM present in our galaxy. As both of these approaches are being used for the same ultimate aim of detecting dark matter, it is interesting to study the complementary reaches of these approaches and how a detection signal from one experiment type could be validated with a signal from the other. In this thesis, we will do just that by simulating hypothetical signals for the respective detection methods and comparing them using statistical methods. We ultimately want to use these simulations to estimate the exposure required for a direct detection experiment to validate a hypothetical dark matter signal at LDMX.

We begin this thesis with a historical overview of dark matter, where we outline the experimental evidence for the existence of dark matter, the most common DM particle candidates and the methods used to search for these particles. The aim and outline of this thesis are given in detail in Section 1.2. In Chapter 2 the theory behind the LDMX signal is discussed and a hypothetical signal is simulated. In Chapter 3 direct detection DM-material interaction rates are derived and used to simulate hypothetical signals. Furthermore, a nested sampling algorithm is used to estimate the underlying model parameters of such a signal. In Chapter 4 the direct detection parameter estimation is projected onto an LDMX-type simulation, which is then used to validate the hypothetical LDMX signal with a statistical hypothesis test. The thesis concludes with future outlook

[1] We refer that the interested reader to Ref. [3]

[2] Note that $c = 1$ in natural units, so mass an energy are given in the same units

and a summary in Chapter 5.

1.1 Overview of Dark Matter

The modern concept of dark matter is rooted in experimental anomalies that were first observed by astronomers centuries ago. Understanding the historical unfolding of the dark matter hypothesis is instructive in introducing the motivation behind and details of the modern research field. In this section, we present an overview of dark matter, beginning with the experimental evidence for its existence, then followed by a discussion of some theoretically appealing candidates, and concluding with the methods used to search for these candidates in the universe.

1.1.1 Evidence for Dark Matter

The concept of unseen dark objects in the sky has been a longstanding challenge for astronomers. Perhaps the earliest known person to postulate the existence of such objects is the German astronomer and mathematician Friedrich Bessel, who in 1844 postulated the existence of faint unseen stars upon the gravitational behavior of Sirius and Procyon [7]. A few years later, new planets were being proposed to explain the anomalous motion of the known planets in the solar system. Uranus was discovered in this way. Another proposed candidate was the dark planet named Vulcan, which would have explained the anomalous perihelia of Mercury [7]. As we know today, Vulcan would never be found. The gravitational behavior of Mercury has instead been explained by the arrival of a new theory of gravity: Einsteins theory of relativity. This historically interesting fact exemplifies the two contemporary theoretical approaches used to explain anomalous gravitational behavior in the Universe today. One approach is to keep the gravitational theory and introduce the existence of an unseen mass, which has led to the modern concept of dark matter. Alternatively, one could claim that no additional matter is needed if we instead alter our gravitational theory, which has led to the modern theory of modified Newtonian dynamics (MOND) first proposed by Milgrom in 1983 [8]. Many astronomical observations have been analysed to determine which of these opposing theories is most promising. Most physicists agree that DM serves as the best explanation for these observations overall, although the debate continues to this day [9].

Arguably the most well-known pioneer of the modern field of dark matter is the Swiss-American astronomer Fritz Zwicky [7]. In 1933, he studied the redshifts of faraway galaxy clusters that exhibited large variations in the apparent velocities of the constituent galaxies. He was the first to apply the virial theorem to these velocities to get an approximation of the galaxy cluster mass. This calculation unveiled a significant discrepancy of roughly one order of magnitude compared to the sum of the visible star-masses within the cluster. A natural explanation for this discrepancy was the proposed existence of some unseen matter, which Zwicky called “dunkle Materie": dark matter. These first calculations were heavily limited by the inaccurate estimates of visible mass and observed parameters such as the Hubble constant, then estimated at $H_0 = 558$ km/s/Mpc [7], which is ~ 10 times larger than the modern estimate of around $H_0 = 67$ km/s/Mpc [4]. Yet, as experimental research has progressed, galaxy cluster observations have become one of the cornerstones of proof for the existence of dark matter.

Another way to study immensely massive astronomical objects like galaxy clusters is to measure the gravitational lensing they give rise to. That is to say, the gravitational pull

that an astronomical clump of mass exerts on light, as explained by general relativity, provides an estimate of the present mass. This estimate can be compared to the visible mass to show a similar discrepancy [7]. One noteworthy gravitational lensing experiment is the Bullet Cluster (1E 0657-56) observation [10]. It observed the collision of two galaxy clusters, which has provided valuable evidence of large scale structure dynamics in the Universe. The visible intracluster plasma, unlike the invisible dark matter, is slowed down in the collision. This can be concluded from the observation, as the visible center of mass gets offset towards the middle of the collision, whereas the mostly dark matter based gravitational lensing center of mass is unaffected. Modified gravitational theories (like MOND) have been particularly poor at explaining this observation [7]. The hypothesis that we solely need to alter our gravitational laws to explain the bullet cluster data has been discarded with a statistical significance of 8σ [11].

Another key part of the experimental evidence for dark matter is galaxy rotation curves. The mass distribution of spiral galaxies can be inferred since the velocity of the stars in a galaxy cannot be higher than the gravitational pull of the galaxy, or else the stars would be flung away into space and the galaxy would dissipate. We expect that this behavior should be well-described by Kepler's third law as

$$v(r) = \sqrt{\frac{GM(r)}{r}} \Leftrightarrow M(r) = \frac{v(r)^2 r}{G} \tag{1.1}$$

where $v(r)$ is the circular velocity of the stars, G is the gravitational constant and $M(r)$ is the mass of the disc galaxy at radius r. However, what measurements show is that Kepler's third law does not hold in this case if we only account for the visible mass in the galaxy; see Figure 1.2. It is observed that the circular velocity mostly stays constant as r increases, instead of falling as $\frac{1}{r}$ as Keplerian motion would predict. If we accept the dark matter hypothesis, the claim is that these galaxies are surrounded by a cloud of dark matter that provides the gravitational force needed to hold the galaxies together, which explains the observations well. It is important to note that the mass discrepancy observed here is the same as for galaxy clusters and gravitational lensing. The fact that multiple physical phenomena all point toward the same explanation provides strong scientific evidence for the existence of dark matter.

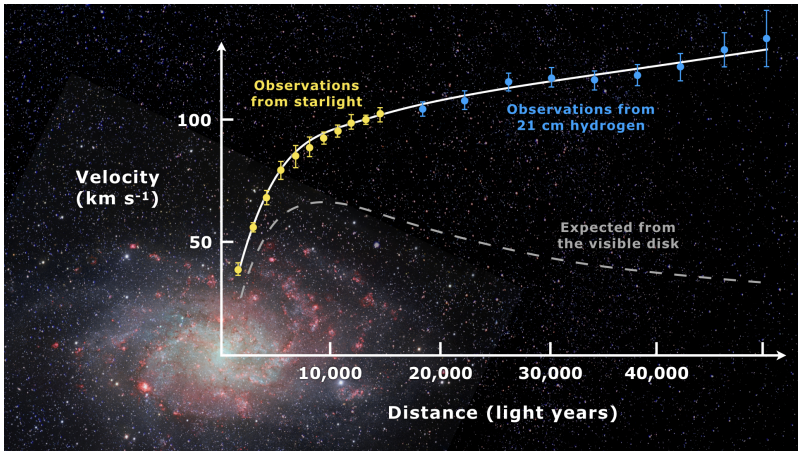

Figure 1.2: A galaxy rotation curve, where the curve expected from the visible light in the galaxy is compared with the one that is observed. Credit: Mario De Leo, CC BY-SA 4.0 https://creativecommons.org/licenses/by-sa/4.0, via Wikimedia Commons.

The last major puzzle piece used to experimentally support the existence of dark matter is the cosmic microwave background (CMB). The CMB consists of photons emitted right after the universe became transparent, and hence the fluctuations in its temperature give insight into the state of the early universe. The temperature anisotropies of the CMB have been measured with great accuracy by the Wilkinson Microwave Anisotropy Probe (WMAP) [12]. By solving the Boltzmann equation for DM present in the early universe, we can use these measurements to predict the evolution of the abundance of dark matter in the universe [13]. Comparing these calculations with the thermal relic observed in the CMB today imposes constraints on the parameter space of dark matter for a given model. Note that these constraints heavily depend upon how DM is presumed to behave. The commonly assumed thermal freeze-out mechanism allows dark matter to be in thermal equilibrium with the SM in the early universe. To reconcile with contemporary abundance observations, it is assumed that the DM decouples from the SM to a stable value of $Y \equiv n/s$ where n is the number of particles and s is the entropy, which happens when the interaction rate drops below the expansion rate of the Universe. The freeze-out hypothesis is used to explain many popular DM candidates, such as Weakly Interacting Massive Particles (WIMPs) and Light Dark Matter (LDM).

1.1.2 Dark Matter Candidates

During the early historical context described in Section 1.1.1 the term "dark matter" originally referred to regular matter that was too faint for the best telescopes to see [7]. The first proposed DM candidates were astronomical objects like brown dwarfs, exoplanets, interstellar gas and so on. As time went on and observational techniques advanced, it was concluded that no ordinary matter could account for the DM anomaly, and so the search had to be redirected towards some yet unidentified type of particle. This is difficult since the only evidence that exists for dark matter is gravitational, which is immeasurably weak at and below atomic scales. Furthermore, the theoretical bounds for the mass of a dark matter particle are immense, ranging from less than a zeV ($\sim 10^{-22}\,\text{eV}$) to hundreds of solar masses ($\sim 10^{68}\,\text{eV}$) [14]. This has given rise to an abundance of theories trying to explain the nature of DM as wavelike fields, weakly interacting particles, primordial black holes and so on.

Standard model neutrinos were proposed as dark matter candidates since they do not interact via the strong or electromagnetic force but instead mainly via the weak force. This would make them a worthy contender, were it not for the fact that neutrinos are very light particles that travel at relativistic velocities. DM candidates traveling at relativistic speeds in the early universe are referred to as Hot Dark Matter (HDM) and candidates with non-relativistic speeds are referred to as Cold Dark Matter (CDM). These two categories result in vastly different formation of large scale structures in the Universe. Simulations of structure formation show that HDM candidates are not reconcilable with observations of current galaxy-sized structures [15]. Note that near relativistic candidates, so called Warm Dark Matter (WDM) candidates, are still explored as a viable option [16]. Even though the standard model neutrino does not constitute dark matter, one can still hypothesize an unseen particle similar to the SM neutrino. These candidates are commonly referred to as sterile neutrinos, which possibly could be the missing right-handed neutrino in the SM [7]. The sterile neutrino would be much heavier than its non-sterile counterpart, making it a valid CDM candidate.

Another popular dark matter candidate has its origins in the strong-CP problem. This is an unsolved issue within the theory of quantum chromodynamics (QCD), which asks

why the Charge and Parity (CP) violating term in the QCD Lagrangian is measured to be very close to zero when there is no theoretical reason for that to be the case. One promising way that this was solved is by introducing a new global U(1) symmetry, which has a corresponding particle called the axion [17]. It was later seen that the axion also fits as a possible DM candidate, hypothetically solving two anomalies with one theory [7]. The axion is a very light (<1eV) dark matter candidate with possible wave-like behavior. The axion exemplifies a common trope for new DM candidates, namely that they often arise as simultaneous solutions to multiple unexplained phenomena. Another well-known example where this is the case are the supersymmetric neutralinos, which would solve many problems in particle physics if proven to exist [12].

While the list of dark matter candidates goes on, the popular scenario where dark matter originates from thermal contact with familiar matter in the early universe puts constraints on DM mass. Weakly Interacting Massive Particles (WIMPS) is a general term for DM particles roughly in the $\sim 1\,\mathrm{GeV}$ to $\sim 100\,\mathrm{TeV}$ scale, which interact via the electroweak force [5]. WIMPs constitute a type of CDM whose self-annihilation cross section matches that of the thermal relic targets very well if the freeze-out mechanism is assumed. Because of theoretical motivations like this and the fact that they lie in the convenient energy range where modern particle colliders like the LHC could probe for them, this has been one of the most studied dark matter types. However, a WIMP has not yet been found. Theoretical and experimental advances in recent years have allowed for a broadening of the search to include DM candidates in other mass ranges [6]. More specifically, an extensive search is now being made for so called light dark matter, which are CDM candidates in the mass range between $\sim 10\,\mathrm{keV}$ to $\sim 1\,\mathrm{GeV}$. The mass range of interest is summarized in Figure 1.3.

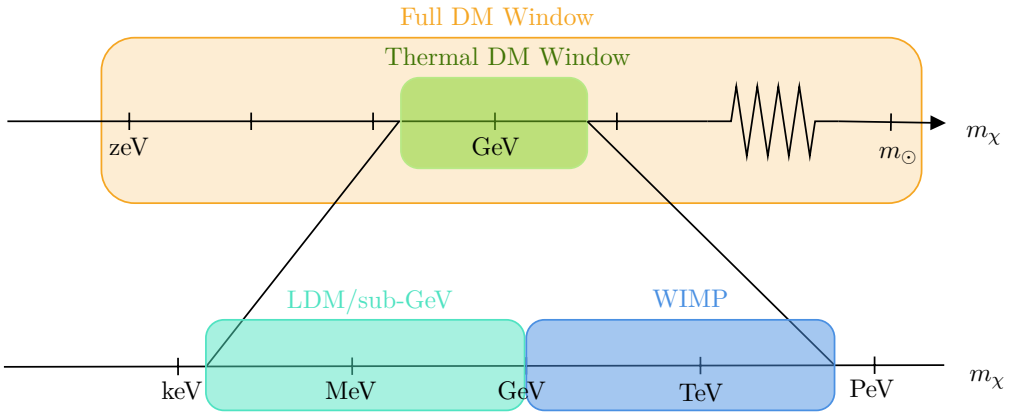

Figure 1.3: The possible mass scale of dark matter candidates, where the light dark matter (LDM) and weakly interacting massive particle (WIMP) mass regimes are highlighted. The thermal window refers to theories that assume the thermal freeze-out scenario, which includes the LDM region considered in this thesis.

When trying to search for dark matter candidates like WIMPs or LDM, assumptions of how the particles could interact with the SM have to be made. This is often referred to in the literature as “portals" to DM, and the options regarding the nature of such a portal are quite extensive [6]. One could assume that DM interacts with the SM directly via a known mediator such as the weak force, which is a relatively simple and predictive scenario. To get a detectable LDM model, it is often necessary to assume that there exists some new mediator particle that interacts both with the SM and with other types of dark

matter. These mediators can be assumed to be massive, and so they could provide part of the mass for all dark matter. Working in these more involved scenarios has introduced the terminology of a “dark sector" as referring to all massive or massless particles that interact with and/or constitute dark matter[3].

In this project, we use a representative model for scalar light dark matter, which is assumed to be mediated by a heavy vector particle referred to as the dark photon, A' [19]. This particle would arise from a U(1) field, analogous to the SM photon, although in the dark sector. This allows for interactions between A' and charged particles in the SM, which are coupled with a newly introduced kinetic mixing parameter ε. We explain this model in more detail in Section 2.1.1.

1.1.3 The Search for Dark Matter

A great deal of theoretical and experimental effort has been put into observing the particle nature of dark matter. Although there is no guarantee that dark matter can be identified in this way, the possibility of detection from such an experiment would provide a monumental leap in our understanding of the Universe.

A multitude of different experiments have been and are being built to monitor certain types of interactions with dark matter. These experiments broadly fall into three categories: direct detection, indirect detection and production at particle accelerators. Each detection type looks for a conceptually different interaction channel between DM and the SM, as is shown in Figure 1.4, and so the experiments are all complementary to each other in exploring DM model parameter space [12].

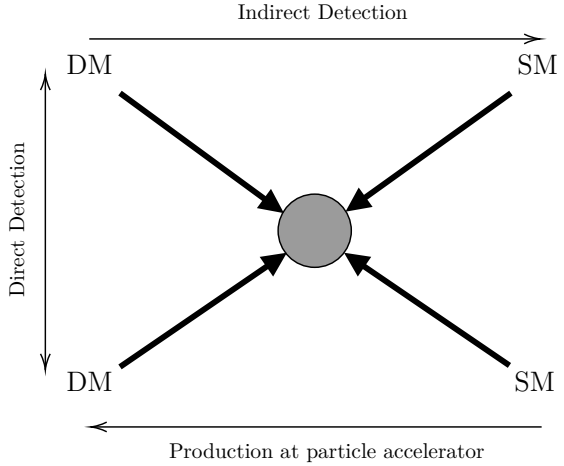

Figure 1.4: An illustration of a generic particle interaction for the three dark matter experiment methods. The four constituent particle types are the same in each case, but the input and output of the observed interactions differ (DM=Dark Matter particle, SM=Standard Model particle).

We discuss each experiment type in more detail below.

[3]See [18] for a review

1.1.3.1 Direct Detection

If we accept the hypothesis that dark matter particles make up a halo around all known galaxies, then they are abundant in the Milky Way. It is expected that a continual barrage of dark matter passes through the Earth as it trails its path through the Milky Way. Direct detection experiments try to monitor faint interactions between this shower of dark matter particles from our local galaxy and the SM matter on Earth. The principle of a direct detection experiment is to gather a large block of some material that is believed to have a high interaction rate with DM, and then try to detect spontaneous reactions like scattering events or lattice excitations in this material. Note that a natural consequence of this setup is that astrophysical parameters like the local density of dark matter in our galaxy are important in these experiments and contribute to uncertainties [20].

The primary interaction being considered in direct detection experiments during the extensive search for WIMPs is the scattering of a DM particle with a nucleon. This approach is unfitting when searching for LDM with sub-GeV mass, as the energy deposited in a nucleus scattering event rapidly drops below detectable limits when the DM mass is lighter than the nucleus mass ($\approx$ a few GeV). Instead, one has to consider other DM-material interactions such as electron scattering, the Migdal effect, DM-phonon scattering and dark photon absorption [21].

The experimental methodology of direct detection in the sub-GeV regime was pioneered by Essig et. al [22]. The methods proposed to find LDM were were both additions to existing experiments based on scintillation's in a noble liquid, and as new experiments based on semiconductor crystal targets. Today, examples of these experiments include Xenon1T [23] [24], LUX-ZEPLIN [25] and Darkside50 [26] that use noble liquid targets (Xe or Ar); or DAMIC [27], SENSEI [28] and CDEX [29] that use semiconductor targets (Si or Ge). This project uses the python package DarkELF [21] to simulate scattering rates for semiconductor crystal type experiments.

1.1.3.2 Detection at particle accelerators

The collision of high-energy particles at accelerators produces a particle shower with the rare chance of containing new exotic particles. Analysis of these experiments has provided experimental verification for many particles of the standard model, and, in theory, dark matter could be detected in the same way [12]. Dark matter would not be seen directly in any of the detectors, similarly to the standard model neutrino, but could still be inferred by accounting for the missing energy or gained transverse momentum of the known particles.

LDMX is a fixed-target collider experiment being built at SLAC national accelerator laboratory [5]. The proposed setup consists of a beam of 4 GeV electrons that are scattered off of a tungsten target and then detected by electronic and hadronic calorimeters. In this setup, the signature of dark matter production is given by incoming beam-energy electrons that are unequivocally associated with low energy, moderate transverse-momentum recoil and the absence of a forward going photon.

1.1.3.3 Indirect Detection

Since our study considers LDM, for which there currently is no method to search for using indirect detection, we do not consider this detection type further in this project. Despite its omission, indirect detection plays a key role in the search for WIMPs and so we briefly

explain it here for the sake of completeness.

The premise of indirect experiments is that dark matter particles could decay or annihilate with each other into detectable SM particles [12]. DM is generally assumed to be stable, making decay exceedingly rare, and so the main process considered is DM-DM annihilation. With the observed abundance of dark matter in far-away galaxies, DM annihilation could presumably produce a flux of excess SM particles that we are able to detect. Indirect detection involves using telescopes to search for a flux of gamma rays, neutrinos, or cosmic rays emanating from galaxies and galaxy clusters that could be attributed to dark matter annihilation. Examples of instruments used to this end include H.E.S.S [30], VERITAS [31], LAT [32] and HAWC [33]. Indirect detection is uniquely useful since dark-matter annihilation scales with the square of its density, making it more sensitive to cosmological and astrophysical processes [12].

1.2 Thesis Outline

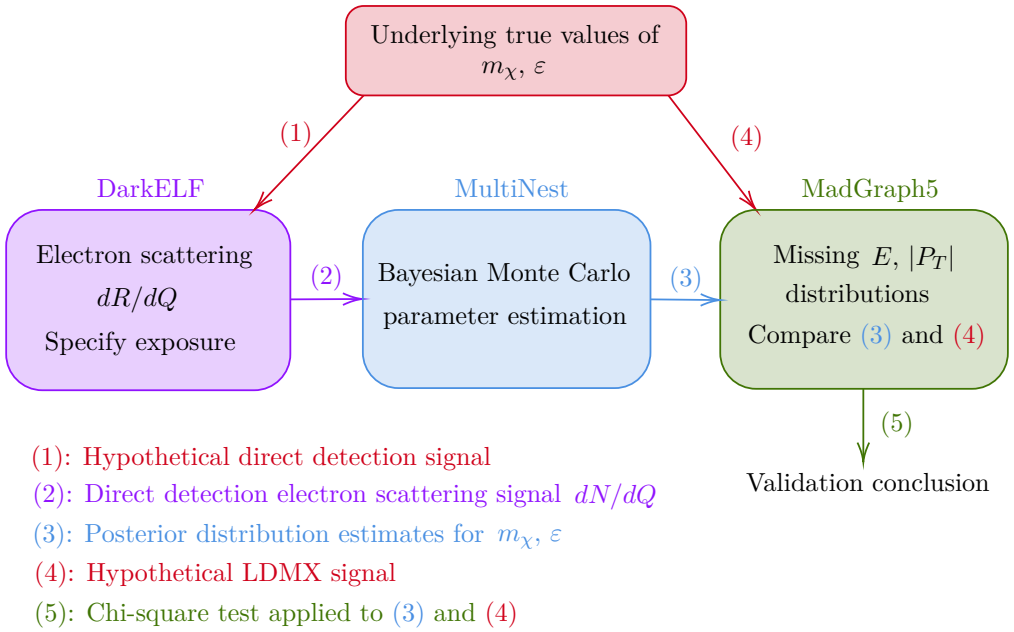

Figure 1.5: An outline of how the three simulation tools that are being utilized in this thesis are used in conjunction. The end goal is to reach a conclusion regarding the validation of an LDMX signal using the parameter estimate from a direct detection signal. The input and output of each simulation tool is briefly explained.

The central question that this thesis aims to answer is the following:

- Given that a dark matter signal is detected at LDMX, how can this signal be validated with direct detection experiments? Specifically, how much exposure is required for a hypothetical direct detection experiment to validate or invalidate a hypothetical LDMX signal at a 95% statistical significance?

This study involves simulating hypothetical experiment data, both for LDMX type experiments using the program MadGraph5_aMC@NLO [34] and for direct detection experiments using the python software package DarkELF [21]. Given the hypothetical direct

detection data, Bayesian parameter estimation will be performed with the MultiNest algorithm [35–37]. In particular, a program adapted to python called PyMultiNest [38] will be used.

In this project, MadGraph5_aMC@NLO will be used to generate plots of the number of signal events as a function of missing energy/transverse momentum. We will primarily explore these distributions' dependence on the DM mass, m_χ, and kinetic mixing, ε, parameters, which are chosen under thermal relic target constraints. These types of figures will then be produced from simulated particle events in the LDMX setup, and will be treated as the result of a hypothetical discovery signal seen at LDMX. Note that this assumption neglects the strenuous challenge of filtering out the SM background from the experiment signal.

DarkELF will be used to simulate direct detection LDM-material interactions. Each simulated signal is an estimate of dR/dQ, which is the scattering rate R binned as a function of the number of ionization electrons Q for a given parameter choice of m_χ and ε. A hypothetical experiment exposure will then be picked and used to obtain the number of events per ionization electron bin: $dN/dQ = dR/dQ \cdot \text{exposure}$. These simulations will be used to produce hypothetical signal data are assumed to follow Poisson distributions.

The hypothetical signal generated from DarkELF will be fitted to a likelihood that is used as input to Multinest. MultiNest is a Bayesian Monte Carlo simulation tool that will be used to sample the posterior distribution of the model parameters, m_χ and ε. These posterior samples will then be used as input to MadGraph to obtain the distribution of missing energy and transverse momentum that we believe LDMX should see given the DD signal. An overview is illustrated in Figure 1.5. Finally, we will apply a chi-square hypothesis test to conclude whether the predicted direct detection distribution and the hypothetical LDMX signal distribution can be consistent. Since the likelihood, and in turn the posterior, depends on the exposure, we will be able to draw a conclusion about the amount of exposure required to make a statistically significant validation of a hypothetical LDMX signal.

2

Simulating a Hypothetical LDMX Signal

The goal of this chapter is to simulate a hypothetical dark matter detection signal at LDMX. To this end, the MadGraph5_aMC@NLO software (henceforth referred to as MadGraph) is used [34].

We start by specifying a representative dark matter model that LDMX has the potential to detect. We consider the interaction channel through which this candidate model would be detected at LDMX and describe how these interactions can be simulated with MadGraph. Finally, different aspects of the MadGraph implementation are discussed and the resulting hypothetical LDMX signals are simulated and shown.

2.1 Light Dark Matter Vector Portal

We outline a representative LDM model and how an LDMX detection signal behaves for this model.

2.1.1 A Representative Dark Sector Model

Throughout this thesis, we work with a simple dark matter model used widely in the community for ease of comparison [14]. The considered model consists of scalar dark matter particles χ with unit charge under an abelian gauge group $U(1)_D$. This abelian group has a corresponding massive vector boson referred to as the dark photon A', which has the coupling $g_D \equiv \sqrt{4\pi\alpha_D}$ to scalar DM currents. Note that χ does not couple to the SM directly in this model. Instead, the portal between the dark sector and the standard model is given by the kinetic mixing term $\propto e\varepsilon$ that arises between the dark photon A' and the conventional photon γ.

The Lagrangian for the considered model, with currents given in the mass eigenstate basis, can be written as

$$\mathcal{L} = \mathcal{L}_{SM} - \frac{1}{4}F'^{\mu\nu}F'_{\mu\nu} + \frac{m_{A'}^2}{2}A'_{\mu}A'^{\mu} - A'_{\mu}(\varepsilon e J^{\mu}_{EM} + g_D J^{\mu}_D) \tag{2.1}$$

where $F'_{\mu\nu}$ is the field strength tensor of A'_{μ}, analogously to in QED, and $J^{\mu}_{EM} = \sum_f Q_f \bar{f}\gamma^{\mu} f$ [6]. We consider the case of scalar elastic dark matter, where $J^{\mu}_D = i(\chi^*\partial^{\mu}\chi - \chi\partial^{\mu}\chi^*)$. This is the simplest way of formulating the dark sector we have discussed, where we notably get a DS portal from the kinetic mixing term $\varepsilon e A'_{\mu}\sum_f Q_f \bar{f}\gamma^{\mu} f$.

We assume specific benchmarking values for two of the model parameters. Firstly, the $\chi - A'$ coupling, represented as $\alpha_D \equiv \frac{g_D^2}{4\pi}$ in analogy with electromagnetism, is set to $\alpha_D = 0.5$.

Secondly, the mass ratio between A' and χ is set to $\frac{m_{A'}}{m_\chi} = \frac{1}{3}$. These values are conservative choices for benchmarking [14]. Setting α_D larger corresponds to stronger experimental sensitivities, i.e. a less constraining exclusion limit, and setting either α_D or $\frac{m_{A'}}{m_\chi}$ smaller similarly overstates the exclusion of thermal relic DM [39]. If these parameters are set too high, it violates unitarity and breaks the consistency of our model [1]. Furthermore, these conservative benchmark choices have been used in previous studies of LDMX [5, 6], which we want to stay consistent with.

It is important to consider the extent to which the model choice limits the general applicability of our conclusions. The benefit of using this model is that it represents a large group of detectable LDM models [6]. Even in the case of a vastly more elaborate dark sector, the kinetic mixing portal, or something resembling it, would often still be present. This simple scenario is also a self-contained, renormalizable theory of dark matter [41]. Note that for the considered model with a vector mediator, the model parameter space has mostly been ruled out for visible dark photon decay [6]. Contemporary DM experiments, including this LDMX study, instead consider the mostly uncharted scenario of invisible dark photon decay.

For an experimental study of LDM, the candidate model needs to be detectable in an LDMX-type experiment and at the same time be consistent with constraints from the CMB. As was previously discussed in Section 1.1.2, the scenario that is commonly proposed to resolve this is the hypothesis of a freeze-out. Here, it is proposed that DM is in thermal equilibrium with the SM in the early universe and later, when the interaction rate drops below the expansion rate of the Universe, the equilibrium cannot be maintained and the particles decouple. This implies that the model parameters, m_χ and ε, are constrained to points in parameter space where the thermal relic abundance in the freeze-out scenario matches that of experimental CMB data. The derivation and simulation of such thermal relic targets is omitted from this study [2]. We instead use previous thermal relic results adapted from Figure 5 in Ref. [5]. The constraint from these thermal relics simplifies our study as every value of m_χ is required to have a single appurtenant value of ε.

Every detail of the model we have specified here will be incorporated into the LDMX simulations in the following sections. We will also implement the same model when simulating a hypothetical direct detection signal in Chapter 3 to remain consistent.

2.1.2 Dark Bremsstrahlung at LDMX

LDMX is a proposed fixed target accelerator experiment that, in its first phase, collides a 4 GeV electron beam with a tungsten target [5]. To infer the production of dark matter, the energy and transverse momentum of recoiling electrons are detected via calorimeters. The main process of interest is the dark bremsstrahlung process, $e\,Z \rightarrow e\,Z\,A'$, where the production of a dark photon, A', has a noticeable impact upon the recoil electron. Following this, an analytical formula is presented for the differential electron scattering rate of this process. Note that this result is not what the MadGraph software uses, as it instead relies on involved calculations and Monte Carlo event generation to estimate integrals for the particles and vertices of the process. Nonetheless, it is useful to derive these approximate analytical relations to get a physical intuition for the process at hand.

Dark photons may be generated in electron-nucleus scattering events analogous to the

[1] See Ref. [40] for details on this unitarity violation
[2] For details, see Refs. [13, 42]

conventional bremsstrahlung process. The Feynman diagram for this process is shown in Figure 2.1. The differences compared to conventional bremsstrahlung are that the dark photon, A', is coupled to the electron as εe and that A' is massive. Note that the scalar DM particle, χ, only interacts with A' and itself, and that we assume that A' annihilates into an invisible pair of χ.

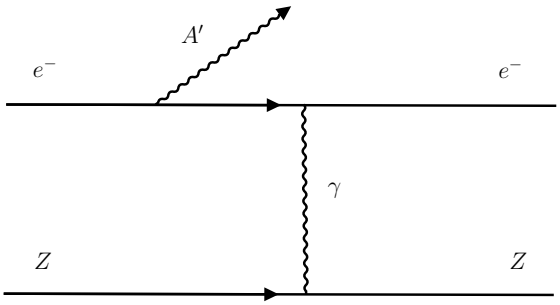

Figure 2.1: The Feynman diagram for dark bremsstrahlung. An incoming electron, e^-, is scattered of a nucleus, Z, (tungsten in the case of LDMX) and a dark photon, A', is created in the process.

This process can be accurately estimated in the Weizsäcker-Williams (WW) approximation, as we show in Appendix A. In essence, the WW approximation treats the nucleus as a cloud of electrons that the incoming electron scatters off of. Under this approximation, an incoming electron with energy E_0 has the following differential cross section to produce an A' [43]

$$\frac{d\sigma}{dx d\cos(\theta_{A'})} \approx \frac{8Z^2\alpha^3\varepsilon^2 E_0^2 x}{U^2}\mathcal{L}og \times \left[(1-x+\frac{x^2}{2}) - \frac{x(1-x)m_{A'}^2(E_0^2 x\theta_{A'})}{U^2}\right] \tag{2.2}$$

where $E_{A'} \equiv xE_0$, Z is the atomic number (74 for tungsten), and $\theta_{A'}$ is the angle between A' and the incoming electron in the lab frame. $\mathcal{L}og \sim 5-10$ (not to be confused with the logarithm operator) depends on the dark matter mass, kinematics, atomic screening and nucleus size [3]. The virtuality of the intermediate electron, U, is given by $U(x,\theta_{A'}) = E_0^2 x\theta_{A'}^2 + m_{A'}^2\frac{1-x}{x} + m_e^2 x$.

A significant consequence of Equation (2.2) is that

$$N \propto \sigma \propto \frac{Z^2\alpha^3\varepsilon^2}{m_{A'}^2} \tag{2.3}$$

where N is the number of events produced in the experiment [43]. This notably implies that $N \propto \varepsilon^2$, which will be of crucial importance in Section 2.2.3.

2.2 Running MadGraph

MadGraph5_aMC@NLO is a thoroughly developed meta code that automatically generates matrix elements for high-energy physics processes [34]. In MadGraph5_aMC@NLO (MadGraph), the MadGraph5 software [44] is used in tandem with the MadEvent package (among others), which uses Monte Carlo techniques to achieve event generation and calculation of cross section for the specified process. The user specifies a certain particle collision

[3] See Ref. [43]

process. MadGraph then generates all Feynman diagrams for the process and outputs the code necessary to evaluate the matrix element at a given phase space point. These matrix elements are evaluated by utilizing helicity wavefunctions and amplitudes.

In the first part of this section, the previously described DM model is incorporated into the MadGraph program. MadGraph is then run to produce histograms that constitute a hypothetical LDMX signal. Next, we outline a method that is implemented to rescale the simulated MadGraph distributions to a physically meaningful total number of events corresponding to the LDMX setup. Finally, we discuss the role of uncertainties in the simulated histograms.

2.2.1 Incorporating the Dark Matter Model into MadGraph

The MadGraph software contains the particles of the SM by default. We also need to add the dark matter particles of interest, namely the dark photon and the scalar dark matter particle. Additionally, the scattering process in LDMX includes a tungsten core, which is made up of SM constituents that are held together by non-trivial QCD interactions. These are theoretically and computationally very difficult to model and implement, so we further introduce a new particle to serve as a simplified approximation of the tungsten nucleus in the LDMX setting.

MadGraph has a framework intended for adding new models beyond the SM, which is done through compatibility with so-called UFO files [45]. These can be generated by the user and include the vertices, new particles, parameters and couplings required to calculate the Feynman rules for the given model. An approximate tungsten core particle is added, which is modeled as a fermion with spin 1/2, an energy equal to the tungsten mass of 171 GeV and an elementary charge of $A = 74$. The dark photon, A', is added as a spin 1 particle with variable mass. A scalar dark matter particle corresponding to χ is added as the invisible product of dark photon decay.

New vertices are explicitly added to model the interactions arising from our DM model. To simulate the bremsstrahlung process of interest, as displayed in Figure 2.1, we need the vertices for tungsten-photon, A'-SM fermion and A'-DM. These vertices include new parameters of relevance, like the A'-SM fermion portal vertex, $\varepsilon e \bar{f} \gamma^\mu f A'$, which introduces the kinetic mixing parameter ε. The A'-DM vertex is also straight-forward to add and has the coupling $\alpha_D = 0.5$. A form factor is also implemented to model the tungsten-photon vertex accurately. The form factor essentially describes how the behavior of the nucleus differs from that of a point-like particle. We describe this as the sum of an elastic and an inelastic component, $G_{2,\mathrm{el}}(t) + G_{2,\mathrm{in}}(t)$, which are given by [43]

$$G_{2,\mathrm{el}}(t) = \left(\frac{a^2 t}{1 + a^2 t}\right)^2 \left(\frac{1}{1 + t/d}\right)^2 Z^2 \tag{2.4}$$

$$G_{2,\mathrm{in}}(t) = \left(\frac{a'^2 t}{1 + a'^2 t}\right)^2 \left(\frac{1 + \frac{t}{4m_p^2}(\mu_p^2 - 1)}{(1 + \frac{t}{0.71GeV})^4}\right)^2 Z \tag{2.5}$$

where $d = 0.164\,\mathrm{GeV}^2 A^{-2/3}$, $a = 111 Z^{-1/3}/m_e$, $a' = 773 Z^{-2/3}/m_e$, m_p is the proton mass and $\mu_p = 2.79\,\mathrm{GeV}$. $t \equiv -q^2$ where q is the difference between the initial and final four-momentum of the nucleus, $q = P_i - P_f$ [4]. The elastic form factor, $G_{2,\mathrm{el}}(t)$, dominates for most $m_{A'}$ we consider, although it is suppressed for larger masses where the inelastic form

[4] See Appendix A for more details

factor, $G_{2,\text{in}}(t)$, dominates instead [43]. The inelastic term holds to a good approximation when t/m_p^2 is small, which is the case here.

2.2.2 Recreating LDMX results

MadGraph is used to generate events for the dark bremsstrahlung process, $e\ Z \to e\ Z\ A'$. The detection of this dark photon process is inferred from studying the outgoing recoil electron. We primarily consider the missing energy, E_e, and transverse momentum, $|P_T|$, of recoil electrons in alignment with the LDMX setup. The resulting number of generated events is displayed as histograms in terms of the observable recoil electron variables, $N(E_e)$, $N(|P_T|)$; see Figure 2.2. These distributions are used to represent the hypothetical dark matter detection signal at LDMX. To produce these figures, we have generated $N_{MG} = 10^4$ dark bremsstrahlung events for the collision of a 4 GeV electron beam with a fixed tungsten target. The dark photon mass dependency of these distributions is also explored, as they are produced for $m_{A'} = 10$, 100, 200, 500, 1000 and 1500 MeV.

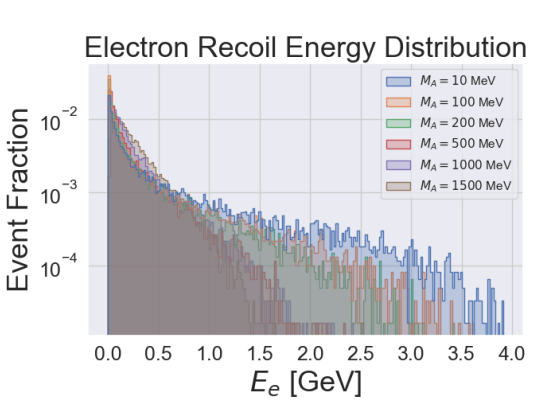

(a) Recoil electron missing energy distributions.

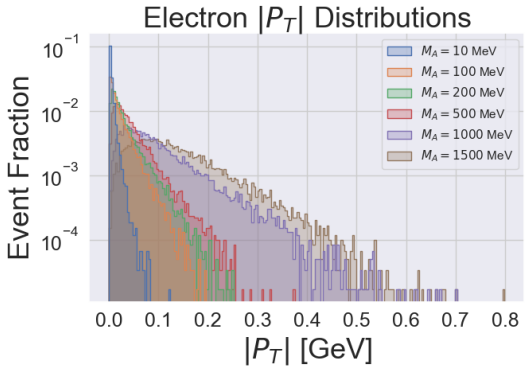

(b) Recoil electron transverse momentum distributions.

Figure 2.2: Distributions of the missing energy and transverse momentum of the recoil electrons in an LDMX-type experiment. These plots are generated from a MadGraph simulation and are intended to reproduce the result of Figure 10 in Ref. [5]. The electron beam is simulated with an energy of 4 GeV and a tungsten target, which corresponds to phase 1 of LDMX.

Notice that the y-axis in Figure 2.2 is normalized to the fraction of events rather than the full event count. This is because the scale of these plots is not of interest yet and simply follows the arbitrary choice of $N_{MG} = 10^4$ that has been made. Each distribution needs to be rescaled to correspond to that of the physical process, which is done in Section 2.2.3.

2.2.3 Imposing Kinetic Mixing upon MadGraph Simulations

The resulting distributions of MadGraph simulations, as is seen in Figure 2.2, are tailored to the number of events that the user picked. Recall that we use $N_{MG} = 10^4$. This is useful to guarantee a satisfactory number of events for the intended accuracy, but problems arise with physical interpretation. The kinetic mixing also gets fixed to some unknown value, because N is fixed in this distribution. In the later comparison of Chapter 4 it is imperative that we have the ability to impose a certain kinetic mixing upon the distribution. It is

therefore relevant to discuss how the resulting MadGraph distributions can be rescaled to impose a certain kinetic mixing.

2.2.3.1 Total Number of Events in LDMX

For a generic particle accelerator counting experiment with signal and background events, the number of final states produced in the experiment, N_X, is given by [46]

$$N_X = \frac{N_{candidate} - N_{background}}{\eta}, \tag{2.6}$$

where $\eta = N_{\text{sel}}/N_{\text{gen}}$ is the experiment efficiency. Note that our simulations assume that the background has already been dealt with, and so we only consider $N_{exp} \equiv N_{candidate} - N_{background}$.

The cross section of the process, σ_X, is defined such that

$$\dot{N}_X = \phi\sigma_X, \tag{2.7}$$

where the flux, ϕ, is the number of collisions per unit time and surface. To determine the cross section we rewrite Equation (2.7) as $\sigma_X = \frac{\dot{N}_X}{\phi}$, and we also integrate these over time to get the relation

$$\sigma_X = \frac{N_X}{\int \phi dt} = \frac{N_{exp}}{\eta \int \phi dt}. \tag{2.8}$$

For collider experiments, $\int \phi dt = \int \mathcal{L} dt$, which is known as the integrated luminosity. The integrated luminosity is conventionally referred to only as the luminosity and is denoted L for convenience. Using this notation, we rewrite Equation (2.8) as

$$N_{\text{exp}} = \sigma L \eta. \tag{2.9}$$

Studies of the LDMX setup use benchmark values for the integrated luminosity and experiment efficiency, namely $L = 4 \times 10^{14}\,\text{EOT}$ (for phase 1) and $\eta = 0.5$ [5]. Note that these are approximate estimates that do not fully incorporate background processes and dependencies on parameters.

The Electrons On Target (EOT) unit of the integrated luminosity is related to cm^{-2} as $L = \text{EOT} \times T \times N$, where T is the target thickness assumed to be $0.1 * X_0 = 0.035\,\text{cm}$ and N is the number density that for tungsten is given by $N = \rho(W)/m(W) = (19.3\,\text{g/cm}^{-3})\,/(3 \times 10^{22}\,\text{g}) = 6.4 \times 10^{22}\,\text{cm}^{-3}$. So the integrated luminosity is $L = 4 \times 10^{14}\text{EOT} = 4 \times 10^{14} \times 2.24 \times 10^{21}\,\text{cm}^{-2} = 8.96 \times 10^{35}\text{cm}^{-2}$.

2.2.3.2 Rescaling MadGraph Generated Distributions

We want to rescale the arbitrarily chosen total number of events, N_{MG}, to impose a kinetic mixing parameter corresponding to that of the thermal relic target constraints. This is applied manually to the generated MadGraph distributions by using Equation (2.9). This formula can be used to calculate what the total number of events should be for the imposed kinetic mixing, which can then be used as a reference to rescale the distributions. The number of events in bin i is related to the number of events that MadGraph has generated

in the same bin as

$$N_{i,imposed}(E) = N_{i,MG}(E)\frac{N_{imposed}}{N_{MG}} = N_{i,MG}(E)\frac{\sigma_{imposed}L_{imposed}\eta_{imposed}}{N_{MG}} = \\ = N_{i,MG}(E)\frac{\sigma_{MG}\frac{\varepsilon^2_{imposed}}{\varepsilon^2_{ref}}L_{LDMX}\eta_{LDMX}}{N_{MG}}$$

In practice, a MadGraph run is first performed to calculate σ_{MG} for a reference kinetic mixing $\varepsilon_{\mathrm{ref}}$. For the MadGraph simulation of interest, the rescaling factor, r, is then given by

$$r = \frac{N_{\mathrm{ref}}}{N_{\mathrm{MG}}}\frac{\varepsilon^2_{\mathrm{impose}}}{\varepsilon^2_{\mathrm{ref}}} \tag{2.10}$$

where $N_{\mathrm{ref}} = \sigma_{\mathrm{MG}}L_{\mathrm{LDMX}}\eta_{\mathrm{LDMX}}$, N_{MG} is the amount of samples specified by the user in the MadGraph run of interest and $\varepsilon_{\mathrm{impose}}$ is the kinetic mixing we wish to impose upon this run.

3

Simulating a Hypothetical Direct Detection Signal and Estimating its Parameters

In the initial sections of this chapter, we simulate a hypothetical dark matter signal from a direct detection experiment using a semiconductor target. First, we formulate the scattering rates of direct detection processes for the considered model. The DarkELF [21] is then used to simulate these interaction rates, and hypothetical signals are generated for different experiment exposures.

In the later sections of this chapter, we discuss statistical Bayesian inference methods with the end goal of estimating the model parameters of the generated hypothetical DD experiments. The MultiNest algorithm [36] is used to perform this parameter estimation.

3.1 Light Dark Matter Interactions in a Dielectric Material

The DarkELF package provides a calculation tool for the interaction rates of light dark matter in dielectric materials. This includes several interaction processes such as electron scattering, the Migdal effect, dark matter-phonon scattering and dark photon absorption [21]. In this section we discuss the first two extensively, as both play a role in the $m_{DM} \sim 1 - 1000\,\text{MeV}$ range that LDMX is interested in. The latter two processes are shown to be relevant at the vastly different DM mass scale of $\sim 0.1 - 10$ eV, and so these processes are not considered further in this project.

These processes are applicable to many different models, including the dark photon mediated scalar dark matter model presented in Section 2.1.1, which is used throughout this thesis.

3.1.1 Electron Scattering

One of the underlying formulas used by DarkELF is one that expresses the electron scattering rate in terms of the Energy Loss Function (ELF) and other well-known parameters. This is a useful relation since the scattering rate is one of the main observables of the scattering process and since the ELF can be evaluated as

$$\text{ELF} = \text{Im}\left[\frac{-1}{\epsilon(\omega, \mathbf{k})}\right] \tag{3.1}$$

where $\epsilon(\omega, \mathbf{k})$[1] is the longitudinal dielectric function that depends on the energy, ω, and momentum, $\mathbf{k}$ of the incoming DM particle. The dielectric function is an extensively studied material property that has been measured for various materials [47]. This approach is computationally inexpensive as the bulk of heavy calculations are either precomputed using time-dependent density functional theory (TDDFT) or avoided by fitting experimental data to a Mermin oscillator model.

For the vector dark photon model being considered here, the Hamiltonian of a direct detection electron scattering event is given by

$$H = g_\chi A' \bar{\chi}\chi + g_e A' n. \tag{3.2}$$

In this case, the scattering of dark matter can also be written using the so-called dynamic structure factor, $S(\omega, \mathbf{k})$. This is useful since it treats the incoming dark photon as a perturbation in the electron number density, $n(\mathbf{r},t)$, which allows for the use of linear response theory to formulate the susceptibility, $\chi(\omega, \mathbf{k})$[2]. Furthermore, the susceptibility is directly related to the dielectric function and can also be related to the structure factor by using the fluctuation-dissipation theorem. Taking all of this together, we obtain the relation

$$S(\omega, \mathbf{k}) = \frac{k^2}{2\pi\alpha} \frac{1}{1 - e^{-\beta\omega}} \mathrm{Im}\left(\frac{-1}{\epsilon(\omega, \mathbf{k})}\right) \tag{3.3}$$

where $\beta \equiv 1/T$ is the inverse temperature and α is the fine-structure constant. Equation (3.3) is a well-known result in condensed matter physics [47].

To extract the DM-electron scattering rate, we consider dark matter coupling to the electron density perturbation through the mediator A'. Applying Fermi's golden rule in this context and then using Equation (3.3) yields the final DM scattering rate in units of the number of counts per unit of exposure as

$$\begin{aligned} R = & \frac{1}{\rho_T} \frac{\rho_\chi}{m_\chi} \frac{\bar{\sigma}_e}{\mu_{\chi e}^2} \frac{\pi}{\alpha} \int d^3v f_\chi(v) \int \frac{d^3\mathbf{k}}{(2\pi)^3} k^2 |F_{DM}(k)|^2 \int \frac{d\omega}{2\pi} \frac{1}{1 - e^{-\beta\omega}} \\ & \times \mathrm{Im}\left[\frac{-1}{\epsilon(\omega,\mathbf{k})}\right] \delta\left(\omega + \frac{k^2}{2m_\chi} - \mathbf{k}\cdot\mathbf{v}\right) \end{aligned} \tag{3.4}$$

where $\mu_{\chi e} = \frac{m_\chi m_e}{m_\chi + m_e}$, ρ_T is the target density, m_χ is the dark matter mass, ρ_χ is the local DM density taken to be ≈ 0.4 GeV/cm^3 and $f_\chi(v)$ is the DM velocity distribution in the galaxy that is taken to correspond to the Standard Halo Model with $v_{\mathrm{esc}} = 500\,\mathrm{km/s}$, velocity dispersion $v_0 = 220\,\mathrm{km/s}$, and Earth velocity $v_e = 240$ km/s. Note that these astronomical parameters have measurement uncertainties that we neglect.

The effective scattering cross section, $\bar{\sigma}_e$, is defined as [48]

$$\bar{\sigma}_e = \frac{\mu_\chi^2 g_e^2 g_\chi^2}{\pi(\alpha^2 m_e^2 + m_{A'}^2)^2} = \frac{16\pi\mu_{\chi e}^2 \alpha \varepsilon^2 \alpha_D}{(m_{A'}^2 + \alpha^2 m_e^2)^2} \tag{3.5}$$

where $\alpha_D = 0.5$, ε is the kinetic mixing and $m_{A'}$ is the dark photon mediator mass, set to $m_{A'} = 3m_\chi$ in this project. Equation (3.5) can be used to relate $\bar{\sigma}_e$ and ε, which are

[1] The dielectric function, $\epsilon(\omega, \mathbf{k})$, is not to be confused with ε that denotes the kinetic mixing.

[2] This is not to be confused with the scalar DM particle also denoted by χ. Unfortunately, it is difficult to use clearer notation for a project that branches over multiple research field

often used interchangeably in the literature[3].

$F_{\mathrm{DM}}(k)$ is the dark photon form factor given by

$$F_{\mathrm{DM}}(k) = \frac{\alpha^2 m_e^2 + m_{A'}^2}{k^2 + m_{A'}^2}, \tag{3.6}$$

which describes how much the nucleus in the material differs from a point particle. In the massive mediator regime, where $\alpha^2 m_e^2 << m_{A'}^2$ and $k^2 << m_{A'}^2$, the form factor simplifies to $F_{\mathrm{DM}}(k) = 1$. In the massless mediator regime the form factor instead simplifies to $F_{\mathrm{DM}}(k) = \alpha^2 m_e^2/k^2$. This project will predominantly work under the massive mediator regime.

The simulations we perform with DarkELF evaluate Equation (3.4) by estimating the ELF and computing the integrals. The most important takeaway from this equation is how the scattering rate R depends on the dark matter mass, m_χ, and kinetic mixing, ε, since these are the main parameters of interest in this study. A full proof of Equation (3.4) is given in Appendix B and was also formerly derived in [47].

3.1.2 The Migdal Effect

A commonly considered DM interaction process in a material is that a DM particle scatters off of a nucleus. For DM in the WIMP mass range, the dominant process is DM-nucleus scattering, but the likelihood of this process plummets when m_χ is below the mass of the nucleus $\sim$ 1GeV. At these LDM mass scales another effect is significantly more probable to occur, namely the so-called Migdal effect. The Migdal effect describes how a DM particle can interact with a nucleus, whereby the nucleus is excited enough for one or more of its electrons to "shake off" [49]. This process can be detected through the emission of an electron, just like electron scattering. Thus, both of these processes contribute to the same type of detection signal.

The scattering rate of LDM via the Migdal effect in a dielectric material is given by the following formula [49]

$$\begin{aligned} R =& \frac{8\pi^2 Z_{ion}^2 \alpha A^2 \rho_\chi \bar{\sigma}_n}{m_N m_\chi \mu_{\chi n}^2} \int d^3v f_\chi(v) \int d\omega \int \frac{d^3\mathbf{q}_N}{(2\pi)^3} \int \frac{d^3\mathbf{k}}{(2\pi)^3} \frac{1}{k^2} \left[\frac{1}{\omega - \frac{\mathbf{q}_N \cdot \mathbf{k}}{m_N}} - \frac{1}{\omega} \right]^2 \\ & \times \mathrm{Im}\left[\frac{-1}{\epsilon(\omega, \mathbf{k})} \right] |F_{DM}(\mathbf{p}_i - \mathbf{p}_f)|^2 |F(\mathbf{p}_i - \mathbf{p}_f - \mathbf{q}_N - \mathbf{k})|^2 \delta\left(E_i - E_f - E_N - \omega\right) \end{aligned} \tag{3.7}$$

where A is the mass number of the element, m_N is the total mass of the nucleus and $\mu_{\chi n}$ is the DM-nucleon reduced mass. σ_n is the DM-nucleon reference cross section that is used to parametrize the reach. The form factor $|F_{DM}(\mathbf{p}_i - \mathbf{p}_f)|^2$ is here given by

$$F_{DM}(q) = \frac{q_0^2 + m_{A'}^2}{q^2 + m_{A'}^2} \tag{3.8}$$

where $q_0 = m_\chi v_0$.

[3]Notice that the conversion from $\bar{\sigma}_e$ to ε requires a peculiar change of variables, since $\bar{\sigma}_e$ is given in units of cm^2 and m is given in units of eV. Heuristically, we know for a photon that $E = h\nu = hc\kappa$ where E is the energy in eV and κ is the wavenumber given in cm^2. Using hc in the appropriate units (in natural units $c = 1$ and $h = 2\pi\hbar = 2\pi$), we get the conversion factor $1\,\mathrm{eV} = 8065.54\,\mathrm{cm}^2$.

Employing a full quantum treatment to derive Equation (3.7) is lengthy and technical, so we refer the reader to [49] for these details. The importance of Equation (3.7) in this project is that it is the primary formula that the DarkELF package uses to study the Migdal effect [21]. As with electron scattering, DarkELF estimates the ELF with a specified method and then evaluates the integrals to get the rate.

We only consider the Migdal effect in a range of m_χ values between $\sim 30\,\mathrm{MeV}$ and $\sim 1\,\mathrm{GeV}$. Above $m_\chi \approx 1\,\mathrm{GeV}$ nuclear recoil dominates as we enter the WIMP regime. The impulse approximation that is used to derive Equation (3.7) breaks down below $\sim 30 - 50\,\mathrm{MeV}$ as the wavefunction of the ion in the crystal must be accounted for in this regime. This occurs because the DM-nucleus collision at these energy scales is of the same order of magnitude as that of phonon excitations in the crystal [21]. One would need to consider multiphonon processes to account for this, which lies beyond the scope and focus of this project.

The resulting cross section of a Migdal interaction scales proportionally to the reduced mass squared. Additionally, if we recall Section 2.1.1, the vector dark photon has a coupling $\propto e\varepsilon$ with the SM photon and by extension all charged particles. As such, the dark photon scattering off a nucleus with Z protons has an additional factor Z^2 in the cross section. Thus, for the model considered here with scalar LDM and a vector A' mediator, we have the relation [50]

$$\sigma_N = Z^2 \sigma_n\,, \quad \sigma_n = \sigma_e \frac{\mu_{\chi n}^2}{\mu_{\chi e}^2}. \tag{3.9}$$

Putting this equation together with Equation (3.5) is useful as it lets us relate the cross section to the kinetic mixing, ε, which is an important parameter of study in this thesis.

The Migdal scattering rate is highest for semiconductor-based experiments such as SENSEI [28] or DAMIC [27], which is the case considered here. The primary alternative where the Migdal effect occurs is via scintillation and ionization in noble liquid experiments such as XENON1T, which are useful for studying the WIMP regime but are poorly favoured in an LDM comparison [51]. This is primarily the case since the band gap of a semiconductor is roughly 10 to 20 times lower than the ionization threshold in liquid Xenon [48]. Furthermore, semiconductors allow for electronic excitation processes rather than just atomic ionization, which gives more potential for LDM detection [49]. We will see from our simulations in Section 3.2.1 for which ranges of m_χ the Migdal effect dominates over electron scattering and vice versa.

3.2 Running DarkELF

The DarkELF package is used to compute the integrals in Equations (3.4) and (3.7). We also compare the exclusion limits in Section 3.2.1 to conclude which processes and materials are most relevant for the validation of LDMX. This yields the hypothetical direct detection signal that is shown in Section 3.2.2.

A prerequisite to these simulations is acquiring the ELF that Equations (3.4) and (3.7) rely on. The DarkELF package provides several options for this. These are the Lindhard and Mermin methods, which are simplified material models fitted to experimental data, and the GPAW method that uses precomputed results from TDDFT calculations [21]. We found that the most accurate and reliable method for extracting the ELF in the context

of this thesis was the GPAW method, and so this is what is used in the simulations below. The data used for the GPAW ELF is acquired from [52] and [53].

3.2.1 Exclusion Limits

We construct an exclusion limit under the assumption that neither DM nor background events have been observed in an experiment with a certain amount of exposure. Assuming that the sampling follows Poisson statistics, we can construct a 90% certain exclusion limit using $n_{\text{events}} = 2.3$ samples. The rate of the process, $R(\sigma)$, is determined for a given reference cross section, σ_{ref}. Concretely the exclusion limit is thus given by

$$\text{exclusion limit} = \frac{\sigma_{ref} \times 2.3}{R \times \text{exposure}}. \tag{3.10}$$

We construct exclusion limits for a range of dark matter masses, where we use σ as the y-axis and m_χ as the x-axis. These exclusion plots should be interpreted as us being 90% sure that, given the lack of detection in a given process with a given exposure, the DM parameters do not lie above the estimated exclusion limit line.

In Figure 3.1 exclusion limits of our DarkELF simulations are displayed alongside the projected exclusion limit for LDMX. The thermal relic abundance target for our model is shown, on which the true DM parameters must lie if the model is assumed to be correct. We have also included the current exclusion limits set by various experiments such as DAMIC [27], Xenon1T [23] [24], SENSEI [28] and DarkSide50 [26]. This comparison is made for scalar dark matter with a vector (kinetic mixing dark photon) mediator. Note that we use $m_{A'} = 3m_\chi$ and $\alpha_D = 0.5$ to match the assumptions of the MadGraph simulations, which is motivated in Section 2.1.1. Every direct detection experiment is taken in the massive mediator regime.

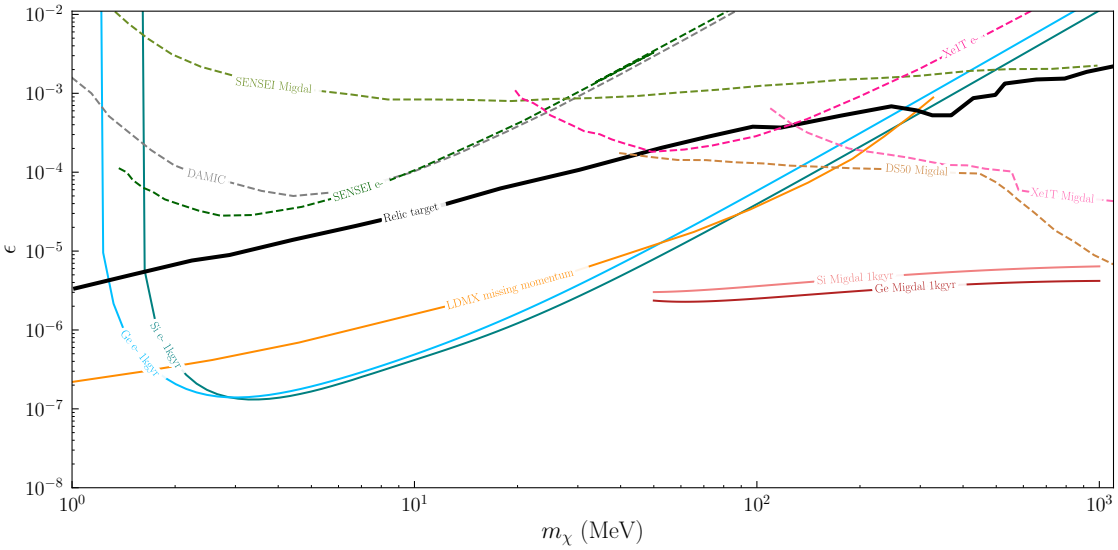

Figure 3.1: Various exclusion limit curves for scalar dark matter with a massive vector mediator. The results from DarkELF calculations using electron scattering (blue lines) and the Migdal effect rates (red lines) are shown and compared using a hypothetical exposure of 1 kg-year. Various experimental exclusion limits are included here for reference. These are the currently available experiment limits of DAMIC [27], Xenon1T [23] [24], SENSEI [28] and DarkSide50 [26]. Note that these direct detection experiments all have different exposures, most only with some tens of g-days.

The point of Figure 3.1 is to compare the exclusion limit of electron scattering and the Migdal effect with that of LDMX. This allows for a discussion of which process is most relevant for validating LDMX for relevant regions of parameter space. Recall that the Migdal effect is expected to dominate for higher masses, whereas electron scattering is dominant for lower masses. This agrees with the DarkELF simulations in Figure 3.1 where the Migdal effect starts dominating over electron scattering at roughly $\sim 30 - 100\,\mathrm{MeV}$. The various experiments in the figure also agree with this principle. Note that in the light mediator regime, which is not relevant for the model we consider, DM-electron scattering dominates for the entire mass range [54]. We conclude from Figure 3.1 that electron scattering is the most relevant process to consider for validation of the LDMX signal. As such we do not consider the Migdal effect when generating the hypothetical signals in Section 3.2.2.

Let us remark why our Migdal simulations are cutoff in Figure 3.1 for masses below 50 MeV. The DarkELF simulation of the Migdal effect relies on the impulse approximation, which treats the recoiling ion wavefunction as a plane wave. This approximation is valid as long as $E_N >> \bar{\omega}_{ph}$, where $\bar{\omega}_{ph}$ is the average acoustic phonon frequency in the crystal [21]. Roughly this lies at several tens of MeV for most materials. This makes it necessary to cutoff simulations below $\sim 50\,\mathrm{MeV}$, as the simulation accuracy deteriorates significantly below that point. Note that it is possible to estimate the rate more accurately below this point by considering multiphonon processes.

3.2.2 Differential Scattering Rate

Proceeding from the electron scattering rate given in Equation (3.4), we can evaluate the differential scattering rate, $dR/d\omega$, by simply moving $d\omega$ to the left-hand side. It is also useful to bin ω in terms of the number of ionized electrons, Q, and evaluate the differential scattering rate as dR/dQ. This yields a discrete distribution where each detected event is binned according to the number of e^-e^+ pairs it created. This function is available in DarkELF for Si and Ge, which are the target materials that are considered in this project [21]. Note that in-medium screening effects automatically are included in the DarkELF calculations (using `withscreening=True`).

Figure 3.2 shows representative results of the differential electron scattering rate dR/dQ binned as a function of the number of ionized electrons Q for DM masses $m_\chi = 10$, 50, 100, and 500 MeV. Excitations are limited to a maximum of 10 Q bins in order to avoid the computational costs associated with the higher-order excitations that have a negligible contribution. This may contribute to approximation errors, which are notably more relevant for higher m_χ.

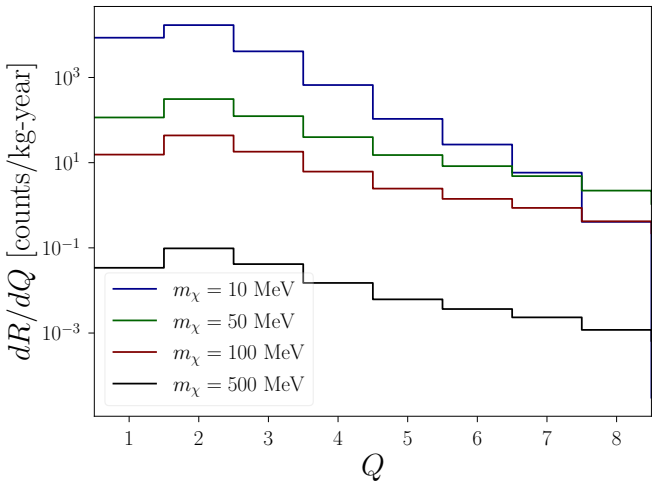

Figure 3.2: Differential electron scattering rate, dR/dQ, of dark photons interacting with a silicon material. The rate is binned in terms of the number of ionized electrons, Q, and the first 10 bins are calculated. It is apparent that the form of this distribution depends on the dark matter mass.

Simulations of the kind shown in Figure 3.2 are used as the basis for the hypothetical direct detection signal. The rate is converted to count as $dN/dQ = \text{exposure} \times dR/dQ$ where we sweep over many values of exposure for comparison. Furthermore, we introduce artificial experimental errors, since we want to treat $\frac{dN}{dQ}$ as a hypothetical direct detection signal. These errors are assumed to follow Poisson statistics, as is known to be the case for counting experiments. For each bin, N_i, we take the hypothetical result as a random sample from the distribution $\text{Poi}(N_i)$. The theoretical mean of this Poisson distribution is N_i and the standard deviation is $\sqrt{N_i}$. This means that the relative errors of the signal samples decrease as N_i gets larger, which is the case for a smaller DM mass[4] and for higher experiment exposure. The fact that these statistical errors decrease as the experiment exposure increases will be crucial for the analysis in Chapter 4.

[4]This is true up to the point of ~ 4 MeV, as is seen in Figure 3.1

3.3 Parameter Estimation with Bayesian Inference

The goal in many fields of research is to produce experimental data that can be used to refute or confirm the current models of the underlying physics. Most particle physics experiments count interaction events at an accelerator, which requires a fundamentally stochastic treatment. The otherwise very useful frequentist methods, such as null hypothesis testing, can often be insufficient in these contexts as the statistical uncertainties are hard to incorporate with frequentist metrics [46]. The methodology of Bayesian statistics provides a natural way of performing a statistical analysis while also including uncertainties independently of their nature [55]. Numerical Monte Carlo methods have become popular for addressing the general problems of parameter estimation and model comparison.

In this section, we switch focus from generating the hypothetical DD signal to analyzing it using Bayesian statistics. We begin with providing a focused introduction to Bayesian inference and the associated methods that will be used in this thesis[5]. Thereafter, we discuss our implementation of the MultiNest algorithm, with the end goal of estimating the underlying DM model parameters, m_χ and ε, of the DD signal.

3.3.1 Bayes Theorem

The two most widely used approaches in the statistics field today are frequentist and Bayesian statistics. These two disagree on a fundamental level: frequentist statistics defines probabilities in terms of frequencies of outcomes, whereas Bayesian statistics defines probabilities as a degree of belief. For instance, the frequentist approach describes model parameters as fixed true values that become apparent in the limit of infinite samples, whereas the Bayesian framework views model parameters as random variables that are described by some probability density function (PDF).

The core of what makes the Bayesian approach useful is Bayes theorem. Bayes theorem follows from the standard axioms of probability theory and states that

$$P(A|B) = P(A)\frac{P(B|A)}{P(B)} \tag{3.11}$$

where $P(A)$ and $P(B)$ are unconditional probabilities of events A and B occurring, while $P(A|B)$ is the probability of A occurring given that B already has occurred [57].

The common procedure is to consider a model, $\mathcal{M}$, with independent model parameters, θ, and a newly collected set of data, D. In this very general scenario, we can formulate Bayes theorem as

$$P(\theta|D,\mathcal{M}) = \frac{P(D|\theta,\mathcal{M})P(\theta|\mathcal{M})}{P(D|\mathcal{M})} \tag{3.12}$$

where $P(\theta|D,\mathcal{M}) \equiv \mathcal{P}(\theta)$ is the posterior, $P(D|\theta,\mathcal{M}) \equiv \mathcal{L}(\theta)$ is the likelihood, $\equiv \pi(\theta)$ is the prior and $P(D|\mathcal{M}) \equiv \mathcal{Z}$ is the Bayesian evidence [57]. The likelihood incorporates how the theoretical model describes the data, whereas the prior incorporates our previous knowledge of the model parameters.

The choice of a prior is often ambiguous as it depends on the information the user has and deems relevant. This subjectivity is usually used as a critique of Bayesian methods, although it can also be found in the assumptions of frequentist methods [58]. For instance, the maximum likelihood estimator implicitly assumes a uniform prior, which in many

[5] See Refs. [56, 57] for extensive reviews

cases contains less information than what is available. In contrast, the Bayesian approach provides a natural way of incorporating assumptions and previous knowledge in a rigorous way. The frequentist approach is much more restricted in this sense, yet it has its own virtues in terms of ease of use and computationally inexpensive metrics.

3.3.2 Parameter Estimation

The posterior Probability Density Function (PDF), $P(\theta|D,\mathcal{M})$, as defined in Equation (3.12), encapsulates an estimate of the degree of belief for the parameters, θ, of a certain model, $\mathcal{M}$, given our prior knowledge about the model and the information contained in the data, D. In other words, $\int_R P(\theta|D,\mathcal{M})d\theta$ yields the probability that the true values of θ lie within the region R. Explicitly, the following formula based on Bayes theorem is used to evaluate the posterior:

$$P(\theta|D,\mathcal{M}) = \frac{P(D,\mathcal{M}|\theta)P(\theta)}{\int P(D,\mathcal{M}|\theta)P(\theta)d\theta}. \tag{3.13}$$

We are often not interested in all the parameters of our complex model but want to focus on a few key parameters. The uninteresting nuisance parameters, ψ_i, can be integrated out, which is a process called marginalization [57]

$$P_{marg}(\theta_1,\ldots,\theta_n|D,\mathcal{M}) \propto \int d\psi_1 \ldots d\psi_m P(\psi_1,\ldots,\psi_n|D,\mathcal{M}). \tag{3.14}$$

The marginal posterior allows for more comprehensible representations as the number of dimensions can be reduced to $n_D = 1,2,3$ where visual representation is possible.

3.3.3 Model Comparison

The role of the evidence, $\mathcal{Z}$, can vary drastically depending on the problem. In parameter estimation, since $\mathcal{Z}$ does not depend on the model parameters, it only amounts to a constant factor that can easily be incorporated by normalizing the posterior. In model comparison, where one aims to select between a set of competing models, the evidence plays a crucial role. In fact, the evidence is the main component that needs to be computed in these cases [57], since two model hypotheses are compared using the ratio

$$\frac{P(H_2|D)}{P(H_1|D)} = \frac{P(D|H_2)P(H_2)}{P(D|H_1)P(H_1)} = \frac{\mathcal{Z}_2 P(H_2)}{\mathcal{Z}_1 P(H_1)}. \tag{3.15}$$

The evidence can be evaluated using the formula

$$\mathcal{Z} = \int \mathcal{L}(d|\theta,\mathcal{M})\pi(\theta|\mathcal{M})d\theta. \tag{3.16}$$

One of the strengths of Equation 3.16 is that it naturally incorporates Occam's Razor: a model that has unnecessary extra parameters is disfavoured due to its larger evidence compared to a simpler model with a more compact parameter space [59].

3.3.4 Monte Carlo Simulation

The difficulty with employing Bayesian methods in practice is the evaluation of multidimensional integrals over the parameter space of a model, which is needed for the Bayesian evidence (Equation (3.16)) and the posterior (Equation (3.13)). Many numerical methods

have been employed to approximately sample these posteriors efficiently, and chief among them are computational algorithms based on Monte Carlo sampling.

In essence, Monte Carlo methods exploit the fact that the statistical behavior of a moving point will eventually pass through every possible location in an ergodic system [56]. This means that a computer that can simulate enough functional computations from a point moving in parameter space will yield a good approximation to the underlying function. If the points of parameter space are sampled in a systematic way and computed using the integral result in each step, then the entire posterior landscape can be evaluated to a good approximation after a sufficient number of samples.

There are many ways of realizing this fundamental Monte Carlo behavior in a practical sampling algorithm. The most popular choice today is Markov Chain Monte Carlo (MCMC), which uses “walkers" that explore points in parameter space by proposing a stochastic step in each iteration and accepting the new point as a sample with a probability proportional to the likelihood [60]. In this thesis, we will use a more recent Monte Carlo method based on nested sampling, which is discussed further in the following section.

3.3.5 Nested Sampling

Nested sampling algorithms are a type of Monte Carlo method that were first proposed by John Skilling in 2004 [61]. The appeal of these algorithms lies in their potential to provide a more accurate and computationally feasible alternative compared to conventional MCMC sampling. In practice, the MultiNest algorithm [36] has successfully been applied to numerous inference problems in astrophysics to perform Bayesian parameter estimation and model comparison [37]. We use the Multinest algorithm by implementing and running the simulation tool bearing the same name. The Python package implementation of this algorithm called PyMultiNest [38] is used. We provide a concentrated review of the MultiNest algorithm below, and refer the reader to the original papers [35, 36, 61] for the full details.

Nested sampling exploits the relation between the likelihood, $\mathcal{L}$, and prior volume to transform the multidimensional evidence into a one-dimensional integral as

$$\mathcal{Z} = \int_0^1 \mathcal{L}(X) dX \tag{3.17}$$

where X is the prior volume defined as $dX = \pi(\theta) d^D\theta$. Since $\mathcal{L}(X)$ is a monotonically decreasing function of X one can evaluate $\mathcal{L}(X_i)$ by sampling a decreasing sequence of X_i. The evidence can then be approximated numerically using standard quadrature methods as a weighted sum

$$\mathcal{Z} = \sum_{i=1}^{M} \mathcal{L}_i w_i \tag{3.18}$$

where w_i is the weight of each sample.

The algorithm evaluates Equation (3.18) by initially choosing N_{active} active points that are drawn from the prior $\pi(\theta)$ so that the initial prior volume is $X_0 = 1$. The samples are sorted based on their corresponding likelihood values, and the smallest sample, with likelihood $\mathcal{L}_0$, is removed from the active set and replaced by a new point that satisfies the constraint $\mathcal{L}_{\text{new}} > \mathcal{L}_0$. This process is repeated at each iteration, requiring the new

sample to satisfy $\mathcal{L}_{\text{new}} > \mathcal{L}_i$, until the entire prior volume has been traversed. Termination of the algorithm is determined at some specified precision of the evidence.

The evidence gets determined in nested sampling from Equation (3.18). At the same time, all resulting samples (active and inactive) can be used to reconstruct the posterior by assigning each point, j, a weight, w_j, according to

$$p_j = \frac{\mathcal{L}_j w_j}{\mathcal{Z}}. \tag{3.19}$$

This makes it possible to perform both parameter estimation and model comparison with this algorithm.

The hardest part of implementing this nested sampling algorithm is drawing samples from the prior within the hard constraint $\mathcal{L} > \mathcal{L}_i$ at each iteration i. This is problematic since it implies that the sample acceptance rate rapidly decreases, vastly increasing the computational cost at later iterations. To remedy this inefficiency, ellipsoidal nested sampling methods approximate the iso-likelihood contour $\mathcal{L} = \mathcal{L}_i$ by a D-dimensional ellipsoid that is determined from the covariance matrix of the current set of active points. New points are then selected from the prior within this ellipsoidal bound until one is obtained that has a likelihood exceeding that of the removed lowest likelihood point. This means that the prior range shrinks in accordance with the increase of $\mathcal{L}_i$, maintaining a feasible sample acceptance rate.

The MultiNest algorithm builds upon ellipsoidal nested sampling by partitioning the full set of N active points and constructing ellipsoidal bounds at each iteration i. Such an efficient nested sampling algorithm using multiple ellipsoids is useful as it is more proficient at identifying multi-modal posteriors. Realizing this algorithm is quite involved. For instance, the overlap of the multiple sampling ellipsoids has to be properly accounted for. We refer the reader to the original paper [36] for a full explanation of how MultiNest achieves this.

3.4 Running the MultiNest Algorithm

The MultiNest simulation tool [36] is used to perform parameter estimation of the hypothetical direct detection signals (recall Figure 3.2) to extract a marginalized posterior PDF over m_χ and ε. In this section, we elaborate on the methodology required to formalise and run the Multinest package in practice. We begin by formulating the prior and likelihood for our task, followed by a discussion regarding the choice of appropriate hyperparameter values. Thereafter, we outline how splining methods can be used to speed up our computations and conclude with presenting and discussing the sampled marginal posterior.

3.4.1 Prior and Likelihood

The necessary input to the MultiNest algorithm is the definition of a Bayesian prior, π, and likelihood, $\mathcal{L}$. We begin by specifying our previous knowledge of the model parameters of interest, m_χ and σ_e, in the prior. This consists of deciding upon appropriate prior ranges for the parameters and then mapping the initially uniform prior distributions of MultiNest to these priors. The most straight-forward prior choice that reflects our ignorance of the parameter order of magnitude is to use log-uniform priors for both parameters. The range of our priors is constrained by the specific methods of our comparison, as DD electron

scattering is expected to predominantly probe the region of $\sim 1\,\text{MeV}$ to $\sim 100\,\text{MeV}$ with a sensitivity that is similar to LDMX. Recall Figure 3.1. For the DM mass we choose the log-uniform prior range

$$\pi(m_\chi) \sim 10^{\mathcal{U}(6,8)}\text{eV}. \tag{3.20}$$

The $\pi(\sigma_e)$ prior follows from the $\pi(m_\chi)$ choice according to the thermal relic target restriction, so we set $\pi(\sigma_e) \sim 10^{\mathcal{U}(-41,-35)}\text{cm}^2$.

We next define an appropriate likelihood that statistically models our signal. Considering the nature of N we would like to treat the likelihood as a Poisson distribution that is centred around the true values given by the (hypothetical) experiment. We can break N up into its individual bins N_i (in dN/dQ) and treat each of these separately. With this in mind, we define the likelihood of a certain bin as

$$\mathcal{L}^{(i)}(N^i_{\text{exp}}|m_\chi,\sigma_e) = \frac{e^{-N_i(m_\chi,\sigma_e)}}{N^i_{\text{exp}}!} N_i(m_\chi,\sigma_e)^{N^i_{\text{exp}}} \tag{3.21}$$

where N^i_{exp} is given from the hypothetical DD experiment and $N_i(m_\chi,\sigma_e)$ is calculated using DarkELF. The total likelihood is thus given by

$$\mathcal{L}(\{N^i_{\text{exp}}\}|m_\chi,\sigma_e) = \prod_i \mathcal{L}^{(i)}(N^i_{\text{exp}}|m_\chi,\sigma_e), \tag{3.22}$$

where $\prod_i$ is the product over all $n_Q = 10$ bins.

It is convenient to work in terms of the log-likelihood due to ease of computation, which for each bin is given as

$$\log(\mathcal{L}^{(i)}(N^i_{\text{exp}}|m_\chi,\sigma_e)) = -N_i(m_\chi,\sigma_e) + N^i_{\text{exp}} \log(N_i(m_\chi,\sigma_e)), \tag{3.23}$$

where the constant term $N^i_{\text{exp}}!$ has been disregarded as it only amounts to a normalization[6]. The total log-likelihood is analogously given by

$$\log(\mathcal{L}(\{N^i_{\text{exp}}\}|m_\chi,\sigma_e)) = \sum_i \log(\mathcal{L}^{(i)}(N^i_{\text{exp}}|m_\chi,\sigma_e)). \tag{3.24}$$

3.4.2 Choosing Hyperparameters

The nested sampling algorithm that is utilized MultiNest has hyperparameters that adjust how the sampling is performed. Among the most important of these are the number of active points, N_{active}, and the maximum efficiency, e [36]. N_{active} determines how many “active" candidate points are considered in the sampling algorithm at each iteration, whereas e determines the fraction of the prior volume that is being sampled. In the MultiNest article, Ref. [36], these parameters are explained in more detail and rough guidelines are given for setting their values.

For parameter estimation it is recommended to use a minimum of $N_{\text{active}} = 50$ and $e = 1$. These values can be increased to get a more accurate convergence or lowered to get a quick heuristic look at the posterior landscape. For our purposes, we deem that the conservative choices of $N_{\text{active}} = 400$ and $e = 1.3$ are appropriate, which will be used throughout this study. It is necessary to confirm that the assigned values of these hyperparameters actually lead to adequate convergence of the MultiNest algorithm. We find, when using these hyperparameter choices, that the true parameter values are estimated well in the posteriors (see e.g. Figure 3.5). Thus, we deem these choices to be satisfactory for our purposes, although it could be warranted in a future study to thoroughly investigate what the optimal choices of these parameters are in this context.

[6]The normalization is unimportant in parameter estimation, but central to model comparison

3.4.3 Reducing the Amount of Likelihood Evaluations

A useful relation specific to this problem is that N_i has a linear dependence on σ_e (recall Equation (3.4) and that $N = \text{exposure} \times R$). This allows us to make a simplification in that $N_i(m_\chi, \sigma_{e,\text{ref}})$ only has to be fully calculated for a single reference cross section, $\sigma_{e,\text{ref}}$, as it then for any other cross section is given by

$$N_i(m_\chi, \sigma_e) = N_i(m_\chi, \sigma_{e,\text{ref}}) \frac{\sigma_e}{\sigma_{e,\text{ref}}}, \tag{3.25}$$

where we set $\sigma_{e,\text{ref}} = 10^{-38}$ as this lies square in the middle of our prior range. Notice that m_χ must be kept constant for Equation (3.25) to hold. This relation could lead to a significant computational speedup, although it is not trivial to utilize the information directly in the MultiNest algorithm. As the algorithm picks new m_χ and σ_e points according to the underlying sampling rules, each sample has a slightly different m_χ; the simplification is invalidated.

The key insight here is that a new DarkELF simulation does not have to be run every time the likelihood function is called, if instead the mass behavior is precomputed on a grid and then fitted to get an approximate function for $N_i(m_\chi, \sigma_e)$. Using this approach for the likelihood is computationally inexpensive as we only need to compute N_i on a single parameter grid for varying m_χ for one choice of $\sigma_{e,\text{ref}}$. In this way, the number of $N_i(m_\chi, \sigma_e)$ computations can be lowered from a couple of thousands (the number of likelihood calls during a MultiNest simulation), to around a hundred (the number of grid points required to get an accurate fit). We should note that this introduces some approximation errors, although these are negligible if an appropriate fitting method and grid size are used.

There is a vast literature of different functional fitting and interpolation methods to choose from. It should be noted that, since we are able to compute $N_i(m_\chi, \sigma_e)$ for any arbitrary point, although at a relatively high computational expense, this is strictly speaking a functional approximation problem rather than an interpolation one [56]. Interpolation methods can nonetheless be used to similar effect in dealing with this problem and do not require any consideration of the specific shape of $N_i(m_\chi, \sigma_e)$. We deem it satisfactory in this case to use a simple interpolation method that has sufficient accuracy.

Cubic splining is a convenient and well-defined interpolation method that we will use throughout this thesis. The benefit of cubic splining is that the interpolation formula is smooth in the first derivative and continuous in the second derivative, both within a given interval and at its boundaries [56]. This ensures a sufficiently accurate interpolation form for most problems, and at the same time that the interpolation is inexpensive to compute as it is proven to always find a solution in $O(N)$ operations.

In Figure 3.3, we show the result of applying cubic splining to $N_i(m_\chi, \sigma_e)$ for a grid of 100 m_χ points between 1 MeV and 100 MeV. Notice that the number of bins that are relevant to consider increases as the mass increases. We have calculated the first six bins in this case, which is sufficient when $m_{\chi,\text{true}} = 10\,\text{MeV}$. The number of bins considered for a given true DM mass is determined by $N_i(m_\chi, \sigma_e) \geq 5$.

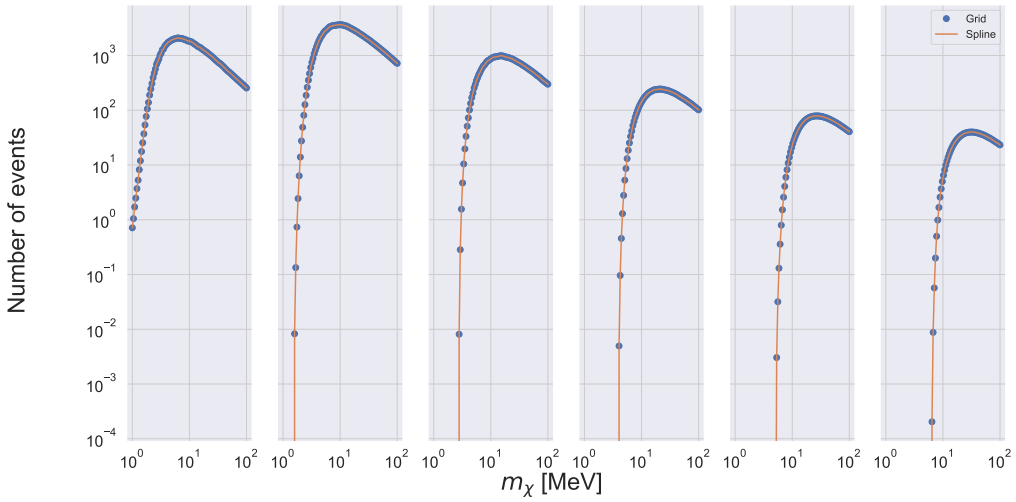

Figure 3.3: The differential number of events dN/dQ for six Q bins of a DD signal is evaluated as a function of m_χ for a log-uniform range of 100 values between 1 and 100 MeV. The values are simulated using DarkELF as previously outlined in Section 3.2.2. Here we have used an exposure of 1 kg-year to get the number of events from the interaction rate.

3.4.4 Posterior Results

The output of the MultiNest algorithm is twofold: The Bayesian evidence Z is calculated, which can be used for model comparison, and the full collection of sampled points can be used to reconstruct the marginal parameter posteriors. We only need to consider the posterior samples in this thesis.

The sampled points are each assigned a weight during sampling according to $p_j = \frac{\mathcal{L}_j w_j}{Z}$, which corresponds to how likely the parameter point is estimated to be, as evaluated by the specified likelihood. The full set of samples can be used to visualize the marginal posterior by plotting the sampled m_χ, ε points in a 2D histogram, although the assigned weight of each sample has to be accounted for. A simple way to do this is to randomly pick a subset of the samples, where each sample has a probability of being accepted proportional to its assigned weight. The resulting subset is referred to as unweighted samples. Concretely, each sample is accepted with a probability of $w_i n_{samples}$, where w_i is the weight of sample i and $n_{samples}$ is the total number of samples. Note that the probability has been scaled by a factor of $n_{samples}$ as to avoid throwing away too many samples[7]. The unweighted samples of a resulting marginal posterior are displayed in Figure 3.4.

[7]Since $\sum_i w_i = 1$ we would otherwise only keep a handful of our many thousands of samples

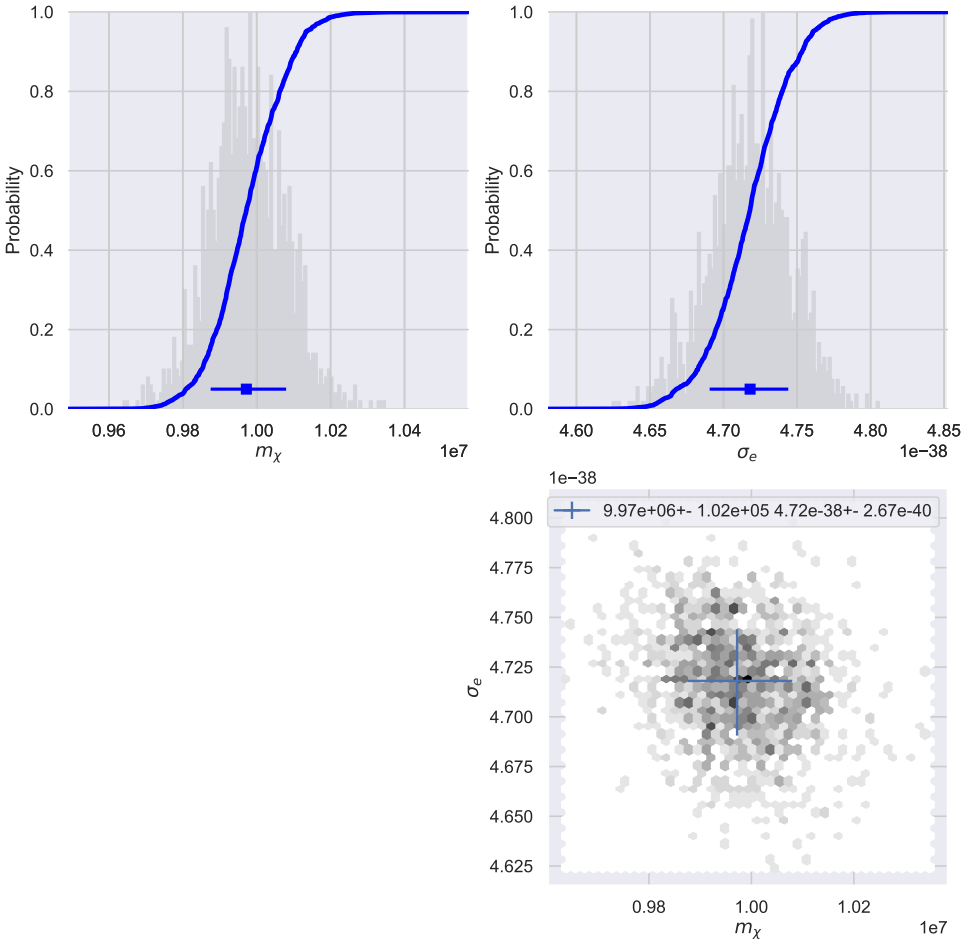

Figure 3.4: Two- and one-dimensional histograms of the marginal unweighted posterior samples from the MultiNest algorithm. This PDF provides an estimate of the model parameters m_χ and $\sigma_e \propto \varepsilon^2$, which is summarized in terms of the distribution mean and standard deviation. To generate the hypothetical DD experiment signal, we have used $m_{\chi,\text{true}} = 10\,\text{MeV}$, implying that $\sigma_{e,\text{true}} = 4.67 \times 10^{-38}\,\text{cm}^2$ from thermal relic constraints, and exposure= 1 kg-year.

The resulting posterior can also be represented in terms of an elliptical confidence region wherein a certain fraction (say 95%) of the samples are located. This ellipse is determined from the covariance matrix of the posterior samples. In Figure 3.5 such confidence regions are shown for three different posteriors that are all based on separate hypothetical experiments with $m_{\chi,\text{true}} = 10\,\text{MeV}$ but with three different exposures of 0.1,1,10 kg-year.

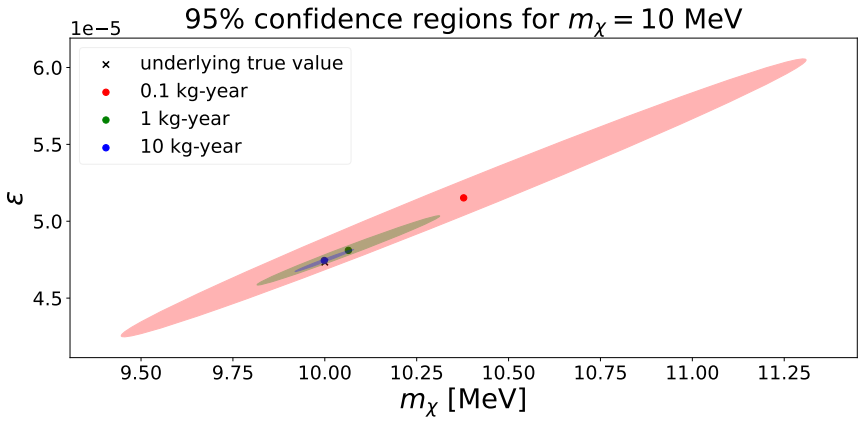

Figure 3.5: 95% confidence region of the posterior probability distribution from MultiNest. We have set $m_{\chi,\text{true}} = 10\,\text{MeV}$ for the hypothetical DD signal. Increasing the exposure of the hypothetical direct detection experiment makes the parameter estimation more certain, and so the confidence region shrinks.

Several comments are in order. Firstly, the posterior PDF exhibits a covariant behavior between m_χ and ε. This is to be expected if we recall Equations (3.4) and (3.6). When $m_{A'}$ gets high enough, in the massive mediator regime we are working with (recall that $m_\chi = 10\,\text{Mev}$ in Figure 3.5 and that $m_{A'} = 3m_\chi$), the form factor, F, approaches 1. This means that the $m_{A'}$ dependence in the integral over momentum space k gets suppressed, and so the relation simplifies to $R \propto \frac{\sigma_e}{m_\chi}$. Since $\sigma_e \propto \frac{\varepsilon^2}{m_{A'}^4}$ and $m_{A'} = 3m_\chi$, this results in a covariant behavior between m_χ and ε in the scattering rate. This behavior is exhibited in the rate simulations and picked up by the likelihood, which results in the strong covariance observed in Figure 3.5.

Secondly, we note that the mean of each distribution always differs slightly from the true underlying value. This is in part due to the inherent stochastic errors of the finite sampling method, although we assume these to be mostly negligible. A more significant source of this effect is the experimental Poisson uncertainty that is introduced to the hypothetical signals. These will be less impactful for larger N as the relative error of a Poisson distribution scales as $\sqrt{N}/N$. This matches what is observed in Figure 3.5 as a larger exposure, implying a larger amount of samples ($N = \text{exposure} \cdot R$), results in a distribution mean that lies closer to the true underlying value.

Lastly, it is also apparent from Figure 3.5 that a larger exposure results in a smaller confidence region. More collected data N (which increases with exposure) results in less relative error (given by $\sqrt{N}/N$ for a Poisson distribution), which in turn results in a more certain PDF sampling from the Bayesian algorithm. In effect, these last two behaviors imply that a higher exposure results in a more certain prediction in the final posterior. This is central to the analysis in Section 4.3.2.

4

Validating the LDMX Signal

In chapter 2 we simulated a hypothetical LDMX signal, and in chapter 3 we simulated a hypothetical direct detection signal and estimated the underlying model parameters, m_χ and ε, from that signal. In the following chapter we tie these simulations together by using the estimated model parameters as input to MadGraph. This gives predicted $N(E)$, $N(|P_T|)$ distributions that represent the signal we believe that LDMX should see given the observed DD signal. Subsequently, this is compared to the hypothetical LDMX result that is generated using the underlying parameter values of $m_{\chi,\text{true}}$, $\varepsilon_{\text{true}}$. A chi-squared hypothesis test is used on these two distributions to conclude if the direct detection signal validates the LDMX signal at 95% statistical significance. By varying the exposure of the direct detection experiment, a conclusion is also drawn regarding the amount of exposure required to validate the LDMX signal. Lastly, we explore how these chi-squared results change if the DD and LDMX signals have been generated for intentionally different underlying parameter values.

4.1 Simulating Direct Detection Predictions in MadGraph

In this section we discuss some aspects that are important when incorporating the parameter estimation into an LDMX prediction with the MadGraph simulation tool.

4.1.1 Incorporating Posterior Samples

It is unfeasible to run an individual MadGraph simulation for each unweighted posterior sample, as the computational cost of simulating thousands of accurate MadGraph runs is far beyond the scope of this project. Cubic spline interpolation, as previously outlined in Section 3.4.3, can also be used here to save on these computational costs significantly. Each bin of the energy and momentum distributions of interest can be interpolated by running MadGraph on a grid of mass points ($1\,\text{MeV} \leq m_\chi \leq 100$ MeV). This spline function is then evaluated for each unweighted posterior sample parameter point at an insignificant computational expense. The contribution of all posterior samples can be summarized as the average and standard deviation of the evaluated spline function in each bin, which gives a single distribution, $N_{DD,i}$, that efficiently incorporates the posterior prediction. Note that this is done for both the recoil energy, E_e, and transverse momentum, $|P_T|$, distributions.

The accuracy of this splining depends on the accuracy of each MadGraph run. To ensure that these errors do not have too large of an impact on the result, we generate 5×10^4 samples for each MadGraph run in the mass sweep. This mass sweep was performed for 20 parameter points log-uniformly distributed between 1 MeV and 100 MeV.

Note that, similarly to what was argued in Section 3.4.3, this splining method is particularly useful here since we only need to compute a one-dimensional grid over m_χ for a single reference kinetic mixing $\varepsilon_{\text{ref}} = 0.01$. Since $N \propto \varepsilon^2$, any other kinetic mixing can be obtained as $N(m_\chi,\varepsilon) = N(m_\chi,\varepsilon_{\text{ref}}) \times \frac{\varepsilon}{\varepsilon_{\text{ref}}}$. Recall the treatment of ε that was derived in Section 2.2.3.

4.1.2 Arbitrary Parameter Choices

With the use of three different simulation tools throughout this thesis, many choices have been made regarding parameter choices that determine the quality, speed or accuracy of the computations. All of these parameter choices are summarized in Table 4.1.

Table 4.1: In each software used in this thesis there are free parameters that have to be specified. We present all of the chosen values here.

Software	Parameter	Value
MadGraph	n_{events}	10000
MadGraph	n_{bins}	30
MadGraph	n_{spline}	20
MadGraph	$n_{\text{realizations}}$	10
MadGraph	$n_{\text{threshold}}$	5
MadGraph	ε_{ref}	0.01
DarkELF	Q_{max}	10
DarkELF	σ_{ref}	$10^{-38}\,\text{cm}^2$
MultiNest	e	1.3
MultiNest	n_{active}	400
MultiNest	n_{spline}	100
MultiNest	$n_{\text{threshold}}$	5
MultiNest	$\pi(m_\chi)$	$1 < m_\chi < 100\,\text{MeV}$
MultiNest	$\pi(\sigma_e)$	$10^{-41} < \sigma_e < 10^{-35}\,\text{cm}^2$

4.1.3 Managing Uncertainties

The simulated results from MadGraph have unavoidable errors that primarily arise due to statistical fluctuations from the Monte Carlo and integration methods used [34]. These errors are less impactful if a sufficient amount of samples, N_{MG}, are generated in each simulation. Determining what constitutes sufficient is subjective, since it is a trade-off between computational cost and accuracy. The issue is further complicated due to the errors having a dependence on the model parameters. We have deemed $N_{MG} = 10^4$ to be a sufficient baseline value that we will use consistently throughout this project. Note that, since N_{MG} is kept the same, the computational errors in each simulation is slightly different depending on the $m_{A'}$ and ε used.

To identify uncertainties, we employ the straight-forward approach of performing the same experiment multiple times and taking the average and standard deviation of all results. Instead of treating the result from one large run directly, we treat it as the average result of 10 runs, each with 1/10 of the total computations. This effectively means that the average numbers we input to our χ^2 test have accuracy and computational cost corresponding to that of $N_{\text{total}} = N_{\text{MG}} \times N_{\text{realizations}} = 10^4 \times 10 = 10^5$ samples. The main virtue of this

method is its ease of implementation and comprehension. We expect that other methods could be used to estimate uncertainty more elaborately, although we deem this to be superfluous in this exploratory study.

In the direct detection prediction, we have one standard deviation from the posterior samples and one from the numerical error in MadGraph. In the error bar figures shown later we add these errors together as

$$\sigma_{\text{tot}} = \sqrt{\sigma^2_{\text{MG}} + \sigma^2_{\text{posterior}}}. \tag{4.1}$$

Note that this does not fully represent all uncertainties that would be present in actual experiment data, such as background events, astrophysical and model parameters, etc.

An aspect of the resulting MG distributions is that bins with the lowest event count have vastly higher relative uncertainty, which arises naturally for Poisson-distributed events. This is highly problematic for the χ^2 test that is outlined in the next section, as it is based on the relative difference between the distributions, which means that these errors have a significant impact on the test results. In short, χ^2 is an asymptotic test that requires a large enough sample size. We impose that $n_{events} \leq 5$ for this reason, and so the first bin that falls below 5, and all bins succeeding it, are cut off from the histograms.

It is important to note that the bins must be equivalent in the two distributions when applying a test metric. As such, the cut-off is chosen based on the full LDMX distribution (for a given DM mass) and then applied consistently to all distributions in the comparison. This implies that the minimum number of counts requirement, $n_{events} \leq 5$, does not necessarily hold for the direct detection distribution, although it is not expected to deviate significantly.

Note that a histogram cut-off results in a small subset of the collected data being disregarded. This removes information from the statistical test, and so one should be careful not to set the cut-off too high. For the number of events and parameter ranges used here we find this effect to be insignificant.

4.2 Hypothesis Testing

Hypothesis testing has a broad range of applications within statistical data analysis. In the general procedure one formulates and computes some statistic that describes a hypothesis about the data. If the statistic falls within a unlikely range, above a large p-value, the null hypothesis is rejected at some statistical significance, concluding that the hypothesis likely is incorrect [56]. One must be careful to note that if the null hypothesis is not rejected, that does not prove that the hypothesis is true. only that it is still consistent with the data present.

When analyzing multiple data sets from a counting experiment, a commonly posited null hypothesis is to posit that the two data sets are drawn from the same distribution function. We are interested in using such a hypothesis test to determine whether the two distributions we generate, $N_{LDMX,i}$ and $N_{DD,i}$, are sampled from the same underlying function. This is the basis for validation in this project.

4.2.1 The Chi-squared Metric

The chi-squared test is a hypothesis test applicable to discrete distributions, such as binned functions or contingency tables [56]. It considers the null hypothesis that the sampled

distribution follows an expected sampling function. Suppose that O_i is the number of events observed in the i th bin and that E_i is the expected number of events in bin i. Note that O_i is always an integer, while E_i might not be. The chi-squared statistic is then given by

$$\chi^2 = \sum_i \frac{(O_i - E_i)^2}{E_i}. \tag{4.2}$$

A larger χ^2 metric indicates that the null hypothesis is less likely, and one could reject that the distribution is sampled from the expected function.

We want to apply the χ^2-test to a fair and consistent representation of the distribution. In this setup we have the freedom to bin our distribution in a way that satisfies this requirement. One of the freedoms is the number of bins (degrees of freedom) we choose to represent each distribution by. If the number of bins is chosen too low, the computation becomes slightly faster but the resolution of the distribution is poor. On the other hand, a high bin count leads to a smoother high resolution histogram, at the expense of increased computational time. With this trade-off in mind we determine that 30 bins give a satisfactory accuracy for our purposes.

The expected number of events, E_i, is most often derived from some theoretical model. This is useful for many applications, but in our case, the expected number of events is given by another observed distribution. This requires a slight alteration of Equation (4.2), as is discussed in the next section.

4.2.2 Are Two Distributions Different?

Consider the case where we have two binned data sets. Let $N_{LDMX,i}$ be the number of events in bin i for the first data set and $N_{DD,i}$ the number of events in bin i or the second data set. We can formulate the chi-squared statistic as [56]

$$\chi^2 = \sum_i \frac{(N_{LDMX,i} - N_{DD,i})^2}{N_{LDMX,i} + N_{DD,i}}. \tag{4.3}$$

Note that we have assumed that two data sets are normalized to the same number of total events. The two data sets in this project are the hypothetical LDMX signal and the predicted experiment signal generated from the parameter estimation of the direct detection data. Calculating this chi-squared test is relatively straightforward, although interpreting its meaning is less so and merits further discussion.

The computed test statistic follows a χ^2 distribution, with a number of degrees of freedom, k, corresponding to the number of bins used. This has an analytically well-defined form that can be integrated. As such, a table of upper and lower tail thresholds can be found in most statistical handbooks (See Ref. [62]). We primarily use the 5% lower critical value for 60 bins, which has a value of 43.188. Henceforth, this will be referred to as the validation threshold for a 95% statistical significance, the meaning of which we clarify below.

The used null hypothesis is the statement that there is no difference between the underlying function of the two distributions. A chi-squared value above the tabulated tail value allows for the rejection of the null hypothesis at that statistical significance. On the contrary, a chi-squared value below this threshold does not prove that the null hypothesis is true; it only shows that the sampled distributions **can** still be consistent with the same distribution function. This formulation is inconvenient for our purposes, since we want to validate that the two data sets are sampled from the same underlying distribution. The best we can

do is claim that they are consistent, and argue that this provides an important initial conclusion regarding the validation of the LDMX signal by using the DD signal.

To further explore the validity of this statistical formulation, we also consider the case where the underlying m_χ and ε values of the two data sets are different. This is done in Section 4.3.3. This represents the scenario where either LDMX or the DD experiment has given a slightly incorrect signal due to systemic errors in the observation setup. The same chi-squared test can be applied, and now with the clear interpretation that the null hypothesis is rejected at a chosen statistical significance.

4.2.3 Rescaled Number of Samples in a Chi-Squared Test

We must consider how the rescaling of the LDMX-generated histograms that was discussed in Section 2.2.3 impacts the χ^2 metric. This rescaling is necessary to impose the kinetic mixing of the posterior samples, and thus it cannot be avoided in our implementation. The DD predicted- and LDMX distributions are rescaled with an overall factor of r_{DD} and r_{LDMX}, respectively, as is given by Equation (2.10). The LDMX distribution has the underlying kinetic mixing $\varepsilon_{\text{true}}$ imposed, whereas the DD distribution has the average of each posterior sample kinetic mixing $\bar{\varepsilon}$ imposed. The overall sample sizes are rescaled as $N_{LDMX,r} = r_{LDMX} N_{LDMX}$ and $N_{DD,r} = r_{DD} N_{DD}$.

The rescaling should be cause for concern since it introduces a normalization shift on the distributions that has a significant impact on the χ^2 metric. We would ideally like to redo the simulation with $N_{MG,new} = N_r$ to get the correct statistical behavior, but this is not computationally feasible for this project. Even with our choice $N_{LDMX} = N_{DD} = 10^4$, the number of samples do match for the two distributions due to different kinetic mixing. Therefore, we need to use a χ^2 formula, similar to Equation (4.3), that works for distributions that have been arbitrarily rescaled. We present a heuristic derivation of this below.

Consider the rescaled distributions $R_i = r_R \bar{R}_i$ and $S_i = r_S \bar{S}_i$ where $\bar{R}_i$, $\bar{S}_i$ are the non-rescaled statistical distributions and r_R,r_S are the rescaling factors. In the null hypothesis that $\bar{R}_i$ and $\bar{S}_i$ are drawn from the same distribution, we estimate the associated probability for bin i as

$$\hat{p}_i = \frac{\bar{R}_i + \bar{S}_i}{\bar{R} + \bar{S}} \tag{4.4}$$

where $\bar{R} \equiv \sum_i \bar{R}_i$ and $\bar{S} \equiv \sum_i \bar{S}_i$. We choose to set $\bar{S} = \bar{R} = N_{MG} = 10^4$ (this is done in the MadGraph simulations for simplicity's sake, although an analogous formula could also be derived for the $\bar{S} \neq \bar{R}$ case). This means that $\hat{p}_i = (\bar{R}_i + \bar{S}_i)/(2N_{MG})$.

The expected number of counts for the rescaled distributions is given by

$$\hat{R}_i = R\hat{p}_i = r_R \bar{R} \hat{p}_i \quad \text{and} \quad \hat{S}_i = S\hat{p}_i = r_S \bar{S} \hat{p}_i \tag{4.5}$$

and the chi-squared statistic summing over all rescaled observations is [56]

$$\chi^2_r = \sum_i \left[\frac{(R_i - \hat{R}_i)^2}{\hat{R}_i} + \frac{(S_i - \hat{S}_i)^2}{\hat{S}_i} \right]. \tag{4.6}$$

We can evaluate the first term in the chi-squared statistic as follows:

$$\begin{aligned}\frac{(R_i - \hat{R}_i)^2}{\hat{R}_i} &= \frac{(R_i - r_R N_{MG}\hat{p}_i)^2}{r_R N_{MG}\hat{p}_i} \\ &= \frac{2N_{MG}}{r_R N_{MG}(\bar{R}_i + \bar{S}_i)}\left(R_i - r_R N_{MG}\frac{\bar{R}_i + \bar{S}_i}{2N_{MG}}\right)^2 \\ &= \frac{2}{r_R(\bar{R}_i + \bar{S}_i)}(r_R\bar{R}_i/2 - r_R\bar{S}_i/2)^2 \\ &= \frac{r_R}{2(\bar{R}_i + \bar{S}_i)}(\bar{R}_i - \bar{S}_i)^2\end{aligned}$$

and the second term in a completely analogous way as

$$\frac{(S_i - \hat{S}_i)^2}{\hat{S}_i} = \cdots = \frac{r_S}{2(\bar{R}_i + \bar{S}_i)}(\bar{S}_i - \bar{R}_i)^2$$

Putting these results together, we get that

$$\chi_r^2 = \sum_i \frac{r_R}{2(\bar{R}_i + \bar{S}_i)}(\bar{R}_i - \bar{S}_i)^2 + \frac{r_S}{2(\bar{R}_i + \bar{S}_i)}(\bar{S}_i - \bar{R}_i)^2 = (r_R + r_S)\sum_i \frac{(\bar{S}_i - \bar{R}_i)^2}{\bar{R}_i + \bar{S}_i}. \quad (4.7)$$

We recognize the sum in Equation (4.7) as the conventional χ^2 metric we are after (recall Equation (4.3)), and so

$$\chi_r^2 = \chi^2(r_R + r_S). \quad (4.8)$$

In practice, this means that the chi-squared metric applied to the rescaled distributions, χ_r^2, has to be scaled by a factor of $\frac{1}{(r_{LDMX}+r_{DD})}$ to obtain the statistically meaningful χ^2.

4.3 Results

In the following section we provide the final result plots of the validation procedure.

4.3.1 Distribution Histograms

In each plot in Figure 4.1 we show two simulated distributions. The first is the hypothetical LDMX signal resulting from a MadGraph simulation with the parameter values $m_{\chi,true}$ and ε_{true}. The second is the DD posterior prediction, where each sample m_χ is incorporated with the splining method described in Section 4.1.1[1], and the ε of each sample is incorporated with the rescaling method described in Section 2.2.3. The DD predicted distribution essentially reflects what we believe that the LDMX signal should be, given the hypothetical DD signal that has been seen. By comparing these distributions with the hypothesis test outlined in Section 4.2, we can draw a conclusion regarding if the DD experiment has validated the LDMX signal.

In Figure 4.1 we show both the distribution of the energy, E_e, and transverse momentum, $|P_T|$, of the recoil electron. The upper plots show a DD predicted signal generated for 1 kg-year exposure, and the lower plots show another signal generated for 0.01 kg-year exposure. These distributions are displayed as error-bar plots, which are constructed from the mean

[1]The splining is performed on a previous MadGraph run over multiple DM masses

and standard deviation of 10 realizations of the distribution. The error bars shown for the DD prediction are the square sum of the posterior sample standard deviation and the 10 MG realizations standard deviation. Both distributions exhibit errors that stem from the MadGraph uncertainty, and for high enough direct detection experiment exposures (1 kg-years in this case), these are primarily the errors we observe. When the DD exposure is low (0.1 kg-years in this case), the posterior uncertainties become significant and make up the main part of the error bars of the direct detection prediction. We apply the χ^2 test outlined in Section 4.2 to the mean of these distributions. These results are what provide the basis for the validation of this thesis. When the exposure is lower, the errors are higher, and so the χ^2 validation result is more uncertain.

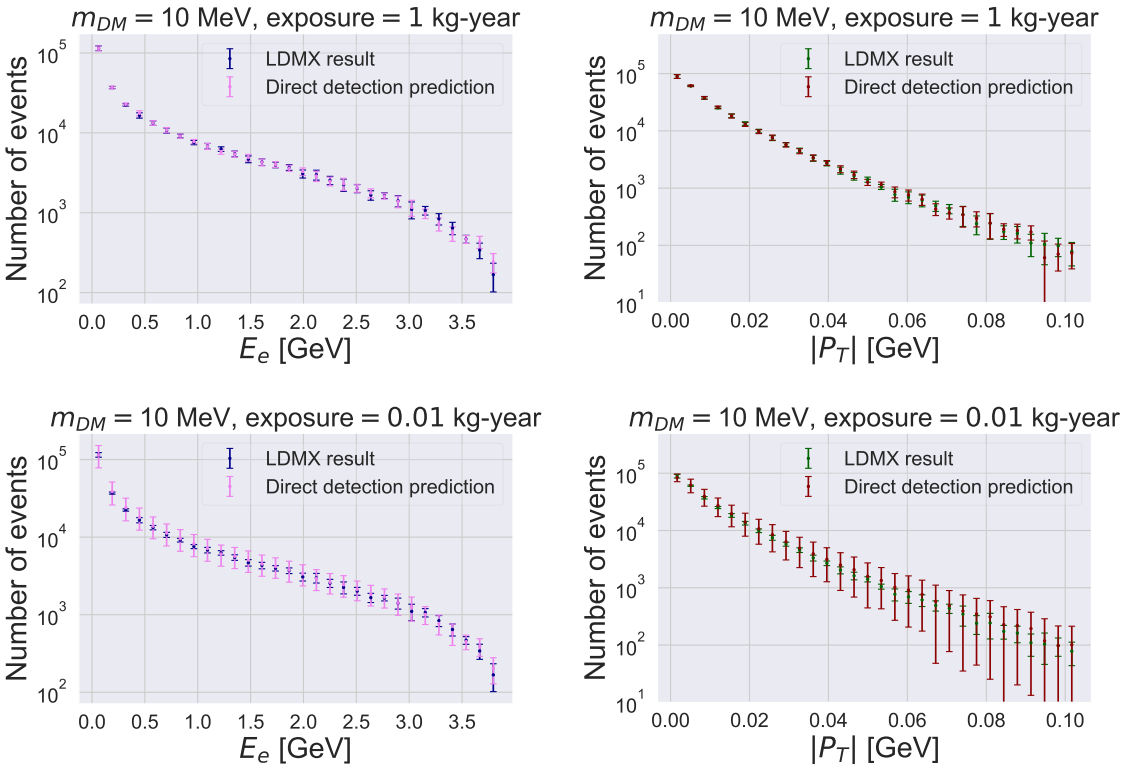

Figure 4.1: In each figure, two MadGraph generated distributions are compared. One uses the underlying true parameter values (LDMX result) and the other uses the parameter values obtained from the MultiNest posterior distribution (Direct detection prediction). In both cases, $m_{\chi,\text{true}} = 10\,\text{MeV}$, which from thermal relic constraints implies that $\varepsilon_{\text{true}} = 4.7 \times 10^{-5}$. The plots to the left show electron recoil energy distributions, whereas the plots to the right show the corresponding transverse momentum distributions. The top figures are for 1 kg-year of exposure in the direct detection experiment, whereas the bottom figures are for 0.01 kg-year exposure. The error bars show the standard deviation of 10 different realizations of these distributions.

Evaluating the χ^2 metric for these distributions and keeping the rescaling factors in mind, we get $\chi^2_E = 4.64$, 43.2 and $\chi^2_{|P_T|} = 5.07$, 48.9 for the 1,0.01 kg-year distributions respectively. The sum of these tests is $\chi^2 = 9.71$ for 1 kg-year and $\chi^2 = 92.1$ for 0.01 kg-year, which can be compared to the 95% confidence validation of 43.19 for 60 degrees of free-

dom. We see that the break point exposure for validation lies somewhere in between 0.01 and 1 kg-year.

4.3.2 Exposure for the Critical Point

The distributions from Figure 4.1 each give a single χ^2 result for the used mass and exposure. As discussed in previous sections (Section 3.4.4 for example), increased exposure decreases the experiment uncertainty and, in turn, gives a more certain χ^2 validation. We would like to determine when the exposure is high enough to give a χ^2 value that consistently validates the LDMX signal with a significance of 95%. In the case that LDMX observes a DM signal, this exposure estimate would provide a rough target for validation with potential future experiments. The break-point exposure depends on the true underlying dark matter mass, if we recall Equation (3.4), and so we explore this exposure sweep for multiple choices of $m_{\chi,\text{true}}$, $\varepsilon_{\text{true}}$.

We start by performing a heuristic sweep over some orders of magnitude of ε for the, $m_{\chi,\text{true}}$, $\varepsilon_{\text{true}}$, choices of interest. This is done to provide a rough guideline for which exposure ranges are relevant to calculate on a dense grid for the different DM mass choices. Thereafter, we can perform a more dense sweep in the exposure range of interest, which for $m_{\chi,\text{true}} = 10\,\text{MeV}$ and $\varepsilon_{\text{true}} = 4.7 \times 10^{-5}$ roughly lies between 0.01 and 1 kg-year of exposure.

In Figure 4.2a the χ^2 metric is calculated for both the missing energy and transverse momentum distributions for 10 different exposures that are log-uniformly distributed between 0.01 and 1 kg-year. We can also incorporate all the information available by simply summing the two χ^2 results, as is shown in Figure 4.2b. Throughout this project, we have used 30 bins for the E and $|P_T|$ histograms, which means that the total χ^2 result is treated as having 60 bins and the 95% confidence level is shown accordingly.

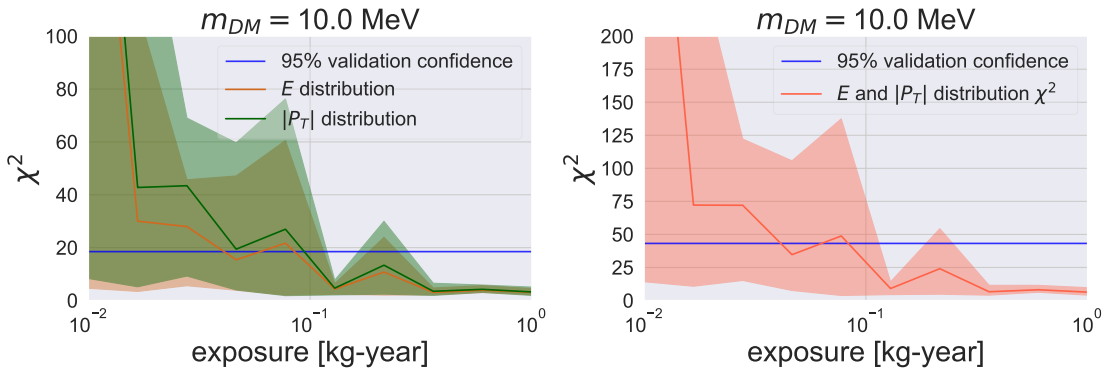

(a) E and $|P_T|$ distribution χ^2 test results for different exposures

(b) Sum of E and $|P_T|$ distribution χ^2 test results for different exposures

Figure 4.2: The result of a χ^2 test applied to the E and $|P_T|$ distributions of LDMX and the direct detection prediction. On the x-axis is the exposure of the direct detection experiment. The left figure shows the E and $|P_T|$ distribution χ^2 results individually (30 dof/bins each), whereas the right figure shows the sum of both results (60 dof/bins total). A stable χ^2 value below 95% confidence is considered a validation of the LDMX signal.

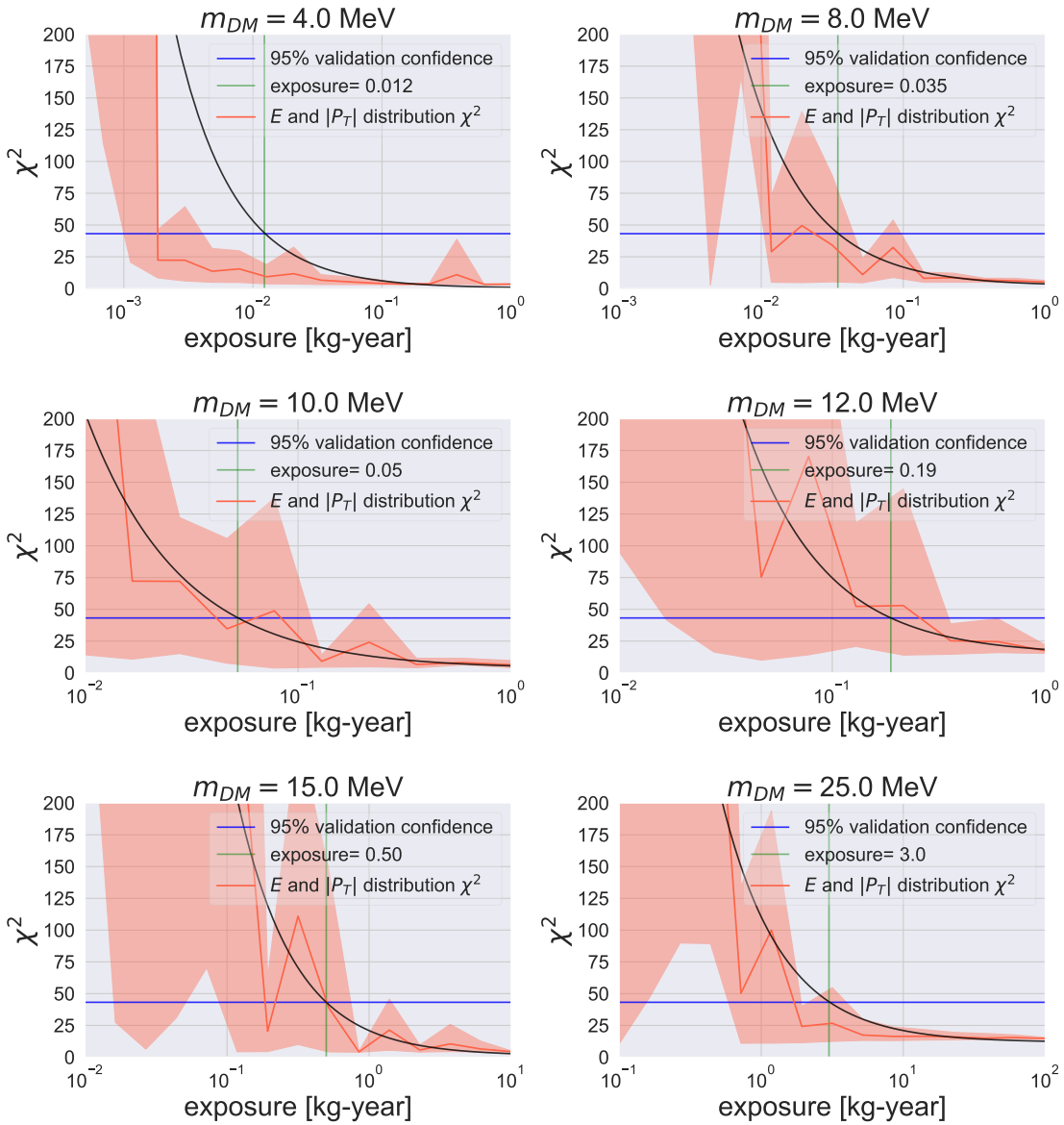

Figure 4.3: The result of a χ^2 test applied to the E and $|P_T|$ distributions of LDMX and the direct detection prediction for varying true dark matter mass. On the x-axis is the exposure of the direct detection experiment. A stable χ^2 value below 95% confidence is considered a validation of the LDMX signal. The black curve in each figure shows the fit of an exponential decay function to the χ^2 means. We mark out the exposure when this fit falls below 95% confidence.

The 95% validation break-point is set to 43.19, as this is the lower-tail 5% critical value of a χ^2 distribution with 60 degrees of freedom. It is unclear where the exact exposure breaking point for validation lies in Figure 4.2. This is partly due to the ambiguity in our χ^2 definition (see the discussion in Section 4.2.2), but also due to the intricate web of uncertainties that underlie these figures. As our way of quantifying uncertainty is through the average and standard deviation of 10 different realizations, the uncertainty region is quite poorly predicted. We want to give a single concrete final exposure value regardless, and we use a simple exponential fit to achieve this. In each plot in Figure 4.3, we fit an exponentially decaying function to the mean of the χ^2 uncertainties as a function of exposure. We mark out the exposure value at the point where the exponential fit falls below the 95% significance of validation. Let us emphasize that this estimate is not a precise, and so it should only be treated as a guideline for future studies.

The DD scattering rate depends on m_χ, and so the validation requires more or less exposure depending on the $m_{\chi,\text{true}}$ that LDMX discovers. We have explored this relation by performing the above analysis for a variety of representative values $m_{\chi,\text{true}} =$ 4, 8, 10, 12, 15, 25 MeV. The result of this is shown in Figure 4.3, where the corresponding break-point exposures are seen to be 0.012, 0.035, 0.050, 0.19, 0.50, 3.0 kg-year. It is seen that a higher value of $m_{\chi,\text{true}}$ requires more exposure for the DD experiment to validate an LDMX signal. We mainly attribute this to the relation first observed in Figure 3.2.1, namely that higher DM masses have less cross section in the direct detection experiment (within the mass range we consider) and so require more exposure to get the same number of counts. This results in a higher relative uncertainty in simulations with higher $m_{\chi,\text{true}}$ for the same exposure, making the χ^2 metric less conclusive.

Factors other than the expected mass dependency could also contribute to the observed results in Figure 4.3. For instance, since we keep n_{MG} constant throughout all runs, simulations with higher $m_{\chi,\text{true}}$ are also more uncertain due to numerical errors in MadGraph. If we examine 3.2.1 and 4.3 more closely, however, we conclude that the mass dependency is the dominant cause of the behavior observed. For instance, consider the graph for $m_{\chi,\text{true}} = 10\,\text{MeV}$, where the validation exposure is 0.05 kg-year, and the one for $m_{\chi,\text{true}} = 25\,\text{MeV}$, where the exposure is 3 kg-year. This is a difference in exposure of roughly two orders of magnitude . Now we see in Figure 3.2.1 that the exclusion limit for 10 MeV is $\varepsilon \simeq 5 \times 10^{-7}$ and for 25 MeV it is $\varepsilon \simeq 5 \times 10^{-6}$. This is roughly a difference of one order of magnitude. This makes sense considering that the exclusion limit is based on the rate, which in turn follows the relation $R \propto \varepsilon^{-2}$ (recall Equation (3.4)). If ε is scaled by a factor of $\sim 10^1$, then R is scaled by a factor of 10^{-2}, and we thus have to increase the exposure by a factor of 10^2 to get the same number of counts ($N = R \times$ exposure). This is the dominant DM mass dependency that is exhibited in the simulations.

All of the results we have produced so far have used silicon as the target material in the direct detection experiment. We also produced the same figures for germanium, although the difference in result was minimal. The resulting figures for this can be found in Appendix C. We conclude that germanium consistently performs slightly worse (requiring more exposure for validation) than silicon in the ranges we have considered. This is consistent with the exclusion limit simulated in Figure 3.1. Considering the exclusion figure, we would also expect that germanium has an advantage for $m_\chi \lesssim 3\,\text{MeV}$, although this has not been verified.

4.3.3 Different True Parameters

In the previous sections, the χ^2-test was always applied to distributions that had originally been simulated for the same underlying true parameters. With the results from these simulations at hand, it is undemanding to also compare distributions that have different underlying true values: $m_{\chi,\mathrm{LDMX}} \neq m_{\chi,\mathrm{DD}}$. This is worth considering as it represents the scenario where significant systematic errors, either in the DD or LDMX setup, lead to perceived parameter values that are significantly different from $m_{\chi,\mathrm{true}}$, $\varepsilon_{\mathrm{true}}$.

Exploring different underlying masses is also insightful for our use of the χ^2 metric. As previously discussed, the validation procedure using the null hypothesis test can never claim anything more than that two distributions can be consistent. In this reverse scenario where we want to claim that the results are different, it is possible to fully utilize the frequentist formulation by rejecting the null hypothesis at some statistical significance. Furthermore, we need to make sure that two noticeably different masses are not still able to successfully validate with our method. If this is the case, then the results of our validation method are meaningless.

In Figure 4.4, the distributions from the hypothetical LDMX and DD distributions are displayed as error bars, similarly to Figure 4.1, but now the parameters $m_{\chi,\mathrm{true}}$, $\varepsilon_{\mathrm{true}}$ are picked to have different values for the two experiments. The true DM mass of the LDMX signal is set to $m_{\mathrm{DM,LDMX}} = 10\,\mathrm{MeV}$, while the true DM mass of the DD signal is set to $m_{\mathrm{DM,DD}} = 8{,}15\,\mathrm{MeV}$. As the difference between 10 and 8 is smaller than between 10 and 15, we notice a more significant difference between the distributions in the latter case. This is also reflected in the χ^2-metric.

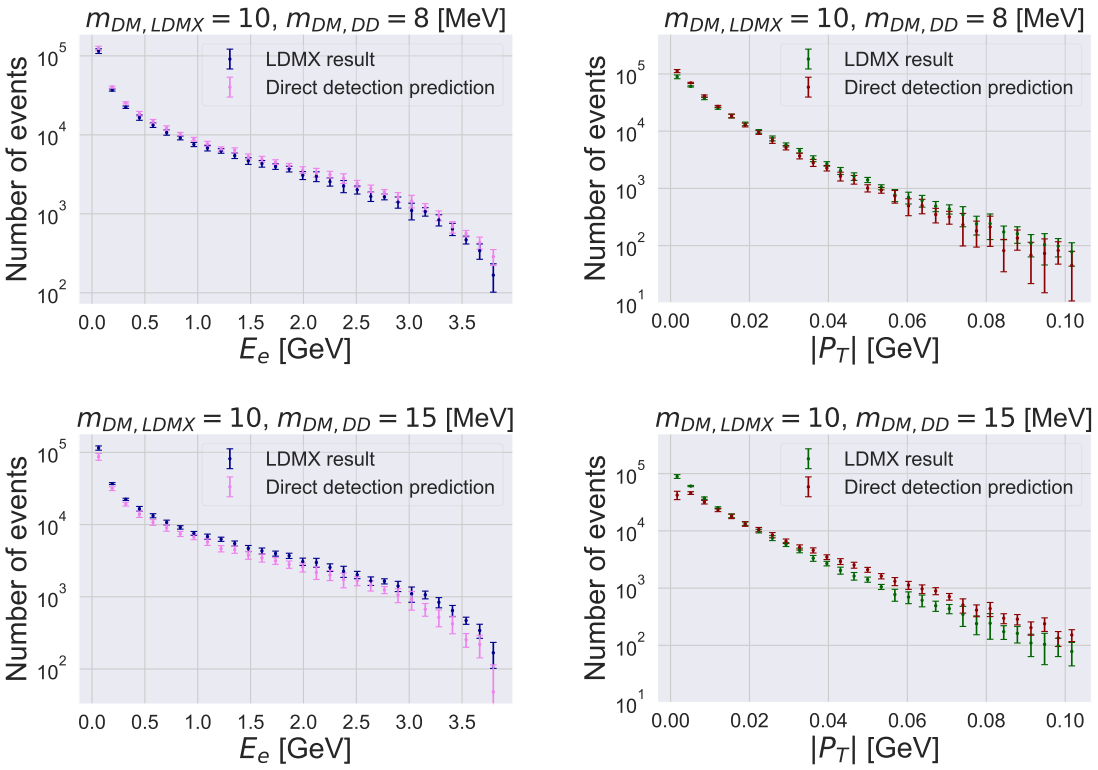

Figure 4.4: Two MadGraph generated distributions are compared in each plot. One uses the underlying true parameter values (LDMX result), which is set to $m_{\mathrm{DM,LDMX}} = 10\,\mathrm{MeV}$ in all cases, and the other uses the parameter values obtained from the MultiNest posterior distribution (Direct detection prediction). The direct detection experiment has different true parameter values than LDMX in this case, specifically $m_{\mathrm{DM,DD}} = 8{,}15\,\mathrm{MeV}$. The plots to the left show electron recoil energy distributions, whereas the plots to the right show the corresponding transverse momentum distributions. The direct detection experiment has 1 kg-year of exposure in all cases here.

In Figure 4.5, the χ^2 result is seen as a function of exposure, similarly to in Figure 4.3, but now the distributions input to the test have different true DM masses. The true LDMX DM mass is kept the same: $m_{\mathrm{DM,LDMX}} = 10\,\mathrm{MeV}$ while the true DD DM mass is varied: $m_{\mathrm{DM,DD}} = 4,\ 8,\ 12,\ 15\,\mathrm{MeV}$. A larger difference in the masses results in a significantly higher χ^2 metric.

The reader should be careful to notice that the 95% upper-tail rejection confidence is not the same as the 95% validation confidence in Figure 4.3. Previously, we argued that a 5% lower-tail confidence implied that the distributions may be consistent with a 95% confidence. In contrast, we here use the 95% upper-tail limit to reject the null hypothesis at that confidence level. This value is 79.08 for a χ^2 distribution with 60 degrees of freedom [62].

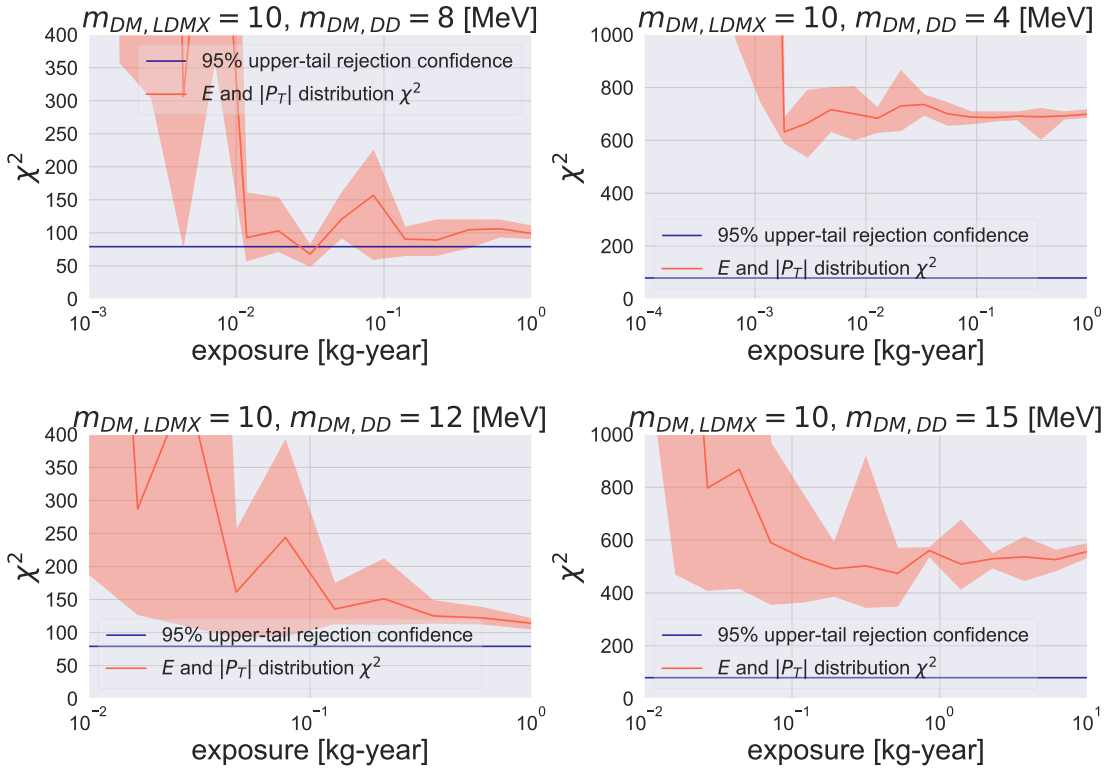

Figure 4.5: The result of a χ^2 test applied to the E and $|P_T|$ distributions of LDMX and the direct detection prediction with different underlying true parameter values. On the x-axis is the exposure of the direct detection experiment. The 95% upper-tail confidence is marked out, above which the null hypothesis that the two distributions are the same can be rejected. As expected, a larger difference in true DM mass results in a more confidently rejected null hypothesis.

5

Outlook and Conclusion

In this chapter, we suggest interesting aspects of this thesis that could be explored in future studies. We conclude by summarizing the developed validation method and offering some final thoughts.

5.1 Future Outlook

While working towards answering the central aim of this thesis, we have discovered many aspects that may be worthwhile to study in more detail. In the following paragraphs, we suggest several extensions to our project that could be interesting to investigate in future studies.

In this project, we have considered a single representative LDM model, namely scalar DM with a massive vector mediator, A'. Many alternative models exist that could be probed similarly by LDMX, such as a scalar or pesudo-scalar mediator or the use of other dipole-moment interaction portals [6]. A future study could exchange the model used here with some of these alternatives and see how the conclusion is affected. Additionally, the MultiNest algorithm provides parameter estimation via posterior samples and simultaneously evaluates the Bayesian evidence, which could be used for model comparison. Such a study could draw conclusions regarding which DM model is most likely to be correct given a hypothetical experiment signal.

The goal in this study was to verify an LDMX signal with DD experiments. One could just as well have drawn a conclusion about validating the hypothetical signal of a DD experiment by using a hypothetical LDMX-type experiment. In such a study, the luminosity of the LDMX-type experiment would be sought after, in analogy to the DD exposure in this study. Further note that the methodology used for validation in this study could be generally applicable to experimental dark matter searches beyond this LDM scenario. It would be straightforward as a first step to tune the simulation parameters of this method to match similar experiments, such as phase 2 of LDMX or other types of LDM DD.

Another approach for validation could be to avoid the frequentist hypothesis test altogether. By performing parameter estimation for both hypothetical signals, two posterior PDFs could be obtained and compared. The benefit of this would be that the errors naturally follow all the way, as is inherent to Bayesian methodology. This would be more thorough than using the crude standard deviation of 10 realizations, which was relied on here. One challenge with taking this approach, however, is to formulate a concrete way of distinguishing when the distributions are consistent at a 95% statistical significance. Unlike with frequentist approaches, where the null hypothesis tests provide well-understood confidence thresholds, we do not know of any corresponding methods for comparing Bayesian

posteriors.

In Chapter 3 we discussed different LDM-material interactions, namely electron scattering and the Migdal effect. It was concluded that electron scattering was most relevant for the study of LDMX, although the Migdal effect could play a large role for DM masses above $\sim 50\,\mathrm{MeV}$. A future study could probe these heavier ranges by also taking into account the Migdal effect in the hypothetical direct detection experiment signal. This would be mostly straightforward to implement, since DarkELF also provides differential scattering rate functions for the Migdal effect, although the binned differential rate, dR/dQ, is not directly available. Other interaction processes, such as multiphonon scattering [21], could also be considered and may prove to have a noticeable impact on the hypothetical signal.

We used the MultiNest algorithm in this study to perform parameter estimation of the direct detection signal. This is a modern MC algorithm developed in the field of astrophysics and has given satisfactory sampling for our purposes. Yet, there is no particular reason for why this algorithm has to be used in this context. A natural alternative choice could be to use conventional MCMC instead [60]. It might be interesting to investigate if MC sampling with a different algorithm like MCMC can give more robust results for a study like this. As a suggestion, such a study could be conducted as a general comparison between the two methods, where the context of this thesis is brought up as one of multiple case studies.

In Chapter 4 we had to resort to rescaling our MadGraph generated distributions with a reference factor, r, to impose a kinetic mixing upon them. This could entail several issues, such as errors being introduced from the reference cross section that is used in the rescaling. Furthermore, there is the issue of statistical applicability and robustness, as it is not trivial to apply a statistical hypothesis test to counting experiment distributions that have been arbitrarily rescaled. If rescaling could be avoided, Hypothesis test metrics other than χ^2 could also be used, such as the Komolgorov-Smirnov test [56]. This is an example of a continuous test that could incorporate more of the information available, thereby resulting in a more robust result.

The simplest way to avoid rescaling is by rerunning the MadGraph simulation with the intended number of samples that the kinetic mixing corresponds to. This was avoided in our study as it requires a computational cost that, by orders of magnitude, exceeds what was reasonable for this small-scale exploratory project. A future study with access to a computer cluster and well-optimized code could run these simulations in a reasonable time frame. This would also make the computational time of DarkELF and MultiNest less daunting, allowing for a more thorough sweep of parameter space.

Lastly, let us emphasize that the simulated experiment results in this study were generated under ideal conditions. We considered a model that is convenient for detection with the LDMX setup, generating a generous amount of events. We also disregarded all background events that otherwise would reduce the number of accepted events significantly. Furthermore, we did not introduce any experimental errors for the hypothetical LDMX signal. It is therefore warranted to propose a future study where the setup is made more realistic by adding background signals and/or choosing a model that generates fewer events in the LDMX signal. This would make the statistical validation harder and perhaps require a more refined methodology to yield clear results. One interesting aspect that would arise if a background signal is added is that the mass dependence of the resulting exposure for validation would be less simple. This is because lower DM masses yield a higher scattering rate and sensitivity, but at the same time background events are most prevalent and

disruptive for these lower DM masses.

5.2 Conclusion

In this project, we implemented a method for validating the dark matter detection signal of LDMX with a semiconductor direct detection experiment for a representative LDM model. Both experiment signals are hypothetical and were generated using the MadGraph and DarkELF simulation tools. The validation procedure consisted of two statistical methods. The underlying DM model parameters, m_χ and ε, were estimated from the direct detection signal using the MultiNest sampling algorithm. This resulted in a posterior distribution that could be used as input to MadGraph to generate a distribution, which represents our degree of belief for the signal that LDMX should observe given the direct detection signal. The χ^2 hypothesis test was then used on the DD predicted distribution and LDMX distribution, which estimated how likely it is that the two distributions are consistent with a single underlying function. When the χ^2 metric fell below the 5% lower-tail threshold we concluded that the LDMX signal is validated at a 95% significance. This entire procedure was repeated many times to determine how much direct detection experiment exposure was required for a 95% validation, depending on the value of $m_{\chi,\text{true}}$. We found that for $m_{\chi,\text{true}} = 4$, 8, 10, 12, 15 and 25 MeV, the required exposure for validation was 0.012, 0.035, 0.050, 0.19, 0.50 and 3.0 kg-year.

The method we developed seems to be a promising way of using a conceptually different direct detection experiment to validate the hypothetical LDMX detection for the considered LDM model. Further development of this method is motivated by the fact that it facilitates future analysis. A robust validation strategy of this kind could prove to be crucial, although not comprehensive, in the event that the long-sought-after dark matter signal is finally found.

References

[1] G. Aad *et al.*, "Observation of a new particle in the search for the standard model higgs boson with the atlas detector at the lhc," *Physics Letters B*, vol. 716, no. 1, pp. 1–29, Sep. 2012, ISSN: 0370-2693. DOI: 10.1016/j.physletb.2012.08.020.

[2] G. Bertone, D. Hooper, and J. Silk, "Particle dark matter: Evidence, candidates and constraints," *Phys. Rept.*, vol. 405, pp. 279–390, 2005. DOI: 10.1016/j.physrep.2004.08.031. arXiv: hep-ph/0404175.

[3] S. Weinberg, *Dreams of a Final Theory*. Knopf Doubleday Publishing Group, 1992.

[4] N. Aghanim *et al.*, "Planck2018 results: Vi. cosmological parameters," *Astronomy and Astrophysics*, vol. 641, A6, Sep. 2020, ISSN: 1432-0746. DOI: 10.1051/0004-6361/201833910.

[5] T. Åkesson *et al.*, "Light Dark Matter eXperiment (LDMX)," Aug. 2018. arXiv: 1808.05219 [hep-ex].

[6] A. Berlin, N. Blinov, G. Krnjaic, P. Schuster, and N. Toro, "Dark matter, millicharges, axion and scalar particles, gauge bosons, and other new physics with ldmx," *Physical Review D*, vol. 99, no. 7, Apr. 2019, ISSN: 2470-0029. DOI: 10.1103/physrevd.99.075001.

[7] G. Bertone and D. Hooper, "History of dark matter," *Rev. Mod. Phys.*, vol. 90, p. 045 002, 4 Oct. 2018. DOI: 10.1103/RevModPhys.90.045002.

[8] M. Milgrom, "A modification of the newtonian dynamics as a possible alternative to the hidden mass hypothesis.," *Astrophysical Journal*, vol. 270, pp. 365–370, Jul. 1983. DOI: 10.1086/161130.

[9] S. S. McGaugh, "A tale of two paradigms: The mutual incommensurability of lcdm and mond," *Canadian Journal of Physics*, vol. 93, no. 2, pp. 250–259, Feb. 2015, ISSN: 1208-6045. DOI: 10.1139/cjp-2014-0203. [Online]. Available: http://dx.doi.org/10.1139/cjp-2014-0203.

[10] A. Robertson, R. Massey, and V. Eke, "What does the bullet cluster tell us about self-interacting dark matter?" *Monthly Notices of the Royal Astronomical Society*, vol. 465, no. 1, pp. 569–587, Oct. 2016, ISSN: 1365-2966. DOI: 10.1093/mnras/stw2670.

[11] D. Clowe *et al.*, "A direct empirical proof of the existence of dark matter," *The Astrophysical Journal*, vol. 648, no. 2, pp. L109–L113, Aug. 2006, ISSN: 1538-4357. DOI: 10.1086/508162. [Online]. Available: http://dx.doi.org/10.1086/508162.

[12] M. Klasen, M. Pohl, and G. Sigl, "Indirect and direct search for dark matter," *Progress in Particle and Nuclear Physics*, vol. 85, pp. 1–32, Nov. 2015, ISSN: 0146-6410. DOI: 10.1016/j.ppnp.2015.07.001. [Online]. Available: http://dx.doi.org/10.1016/j.ppnp.2015.07.001.

[13] P. Gondolo and G. Gelmini, "Cosmic abundances of stable particles: Improved analysis," *Nuclear Physics B*, vol. 360, no. 1, pp. 145–179, 1991, ISSN: 0550-3213. DOI: https://doi.org/10.1016/0550-3213(91)90438-4. [Online]. Available: https://www.sciencedirect.com/science/article/pii/0550321391904384.

[14] M. Battaglieri *et al.*, "Us cosmic visions: New ideas in dark matter 2017: Community report," Jul. 2017.

[15] S. D. M. White, C. S. Frenk, and M. Davis, "Clustering in a neutrino-dominated universe," *Astrophysical Journal*, vol. 274, pp. L1–L5, Nov. 1983. DOI: 10.1086/184139.

[16] S. Paduroiu, Y. Revaz, and D. Pfenniger, *Structure formation in warm dark matter cosmologies: Top-bottom upside-down*, 2015. arXiv: 1506.03789 [astro-ph.CO].

[17] R. D. Peccei and H. R. Quinn, "CP Conservation in the presence of pseudoparticles," *Phys. Rev. Lett.*, vol. 38, pp. 1440–1443, 25 Jun. 1977. DOI: 10.1103/PhysRevLett.38.1440.

[18] R. Essig *et al.*, *Dark sectors and new, light, weakly-coupled particles*, 2013. arXiv: 1311.0029 [hep-ph].

[19] C. Bœhm, X. Chu, J.-L. Kuo, and J. Pradler, "Scalar dark matter candidates revisited," *Physical Review D*, vol. 103, no. 7, Apr. 2021, ISSN: 2470-0029. DOI: 10.1103/physrevd.103.075005.

[20] C. Strege, R. Trotta, G. Bertone, A. H. G. Peter, and P. Scott, "Fundamental statistical limitations of future dark matter direct detection experiments," *Physical Review D*, vol. 86, no. 2, Jul. 2012, ISSN: 1550-2368. DOI: 10.1103/physrevd.86.023507.

[21] S. Knapen, J. Kozaczuk, and T. Lin, "Python package for dark matter scattering in dielectric targets," *Phys. Rev. D*, vol. 105, p. 015 014, 1 Jan. 2022. DOI: 10.1103/PhysRevD.105.015014.

[22] R. Essig, J. Mardon, and T. Volansky, "Direct detection of sub-gev dark matter," *Phys. Rev. D*, vol. 85, p. 076 007, 7 Apr. 2012. DOI: 10.1103/PhysRevD.85.076007.

[23] E. Aprile, J. Aalbers, F. Agostini, *et al.*, "Light dark matter search with ionization signals in xenon1t," *Physical Review Letters*, vol. 123, no. 25, Dec. 2019, ISSN: 1079-7114. DOI: 10.1103/physrevlett.123.251801.

[24] E. Aprile, J. Aalbers, F. Agostini, *et al.*, "Search for light dark matter interactions enhanced by the migdal effect or bremsstrahlung in xenon1t," *Physical Review Letters*, vol. 123, no. 24, Dec. 2019, ISSN: 1079-7114. DOI: 10.1103/physrevlett.123.241803.

[25] J. Aalbers *et al.*, "First dark matter search results from the lux-zeplin (lz) experiment," *Physical Review Letters*, vol. 131, no. 4, Jul. 2023, ISSN: 1079-7114. DOI: 10.1103/physrevlett.131.041002. [Online]. Available: http://dx.doi.org/10.1103/PhysRevLett.131.041002.

[26] 5. Collaboration, P. Agnes, I. F. M. Albuquerque, *et al.*, *Search for dark matter-nucleon interactions via migdal effect with darkside-50*, 2023. arXiv: 2207.11967 [hep-ex].

[27] I. Arnquist, N. Avalos, D. Baxter, *et al.*, "First constraints from damic-m on sub-gev dark-matter particles interacting with electrons," *Physical Review Letters*, vol. 130, no. 17, Apr. 2023, ISSN: 1079-7114. DOI: 10.1103/physrevlett.130.171003. [Online]. Available: http://dx.doi.org/10.1103/PhysRevLett.130.171003.

[28] S. Collaboration, P. Adari, I. M. Bloch, *et al.*, *Sensei: First direct-detection results on sub-gev dark matter from sensei at snolab*, 2023. arXiv: 2312.13342 [astro-ph.CO].

[29] W. H. Dai *et al.*, "Exotic dark matter search with the cdex-10 experiment at china's jinping underground laboratory," *Physical Review Letters*, vol. 129, no. 22, Nov. 2022, ISSN: 1079-7114. DOI: 10.1103/physrevlett.129.221802.

[30] H. Abdalla *et al.*, "Search for dark matter annihilation signals in the h.e.s.s. inner galaxy survey," *Physical Review Letters*, vol. 129, no. 11, Sep. 2022, ISSN: 1079-7114. DOI: 10.1103/physrevlett.129.111101.

[31] B. Zitzer and V. Collaboration, *The veritas dark matter program*, 2017. arXiv: 1708.07447 [astro-ph.HE].

[32] A. McDaniel, M. Ajello, C. M. Karwin, M. D. Mauro, A. Drlica-Wagner, and M. A. Sanchez-Conde, *Legacy analysis of dark matter annihilation from the milky way dwarf spheroidal galaxies with 14 years of fermi-lat data*, 2023. arXiv: 2311.04982 [astro-ph.HE].

[33] A. Albert *et al.*, *An optimized search for dark matter in the galactic halo with hawc*, 2023. arXiv: 2305.09861 [astro-ph.HE].

[34] J. Alwall *et al.*, "The automated computation of tree-level and next-to-leading order differential cross sections, and their matching to parton shower simulations," *Journal of High Energy Physics*, vol. 2014, no. 7, Jul. 2014, ISSN: 1029-8479. DOI: 10.1007/jhep07(2014)079.

[35] F. Feroz and M. P. Hobson, "Multimodal nested sampling: An efficient and robust alternative to markov chain monte carlo methods for astronomical data analyses: Multimodal nested sampling," *Monthly Notices of the Royal Astronomical Society*,

vol. 384, no. 2, pp. 449–463, Jan. 2008, ISSN: 1365-2966. DOI: 10.1111/j.1365-2966.2007.12353.x. [Online]. Available: http://dx.doi.org/10.1111/j.1365-2966.2007.12353.x.

[36] F. Feroz, M. P. Hobson, and M. Bridges, "Multinest: An efficient and robust bayesian inference tool for cosmology and particle physics," *Monthly Notices of the Royal Astronomical Society*, vol. 398, no. 4, pp. 1601–1614, Oct. 2009, ISSN: 1365-2966. DOI: 10.1111/j.1365-2966.2009.14548.x.

[37] F. Feroz, M. P. Hobson, E. Cameron, and A. N. Pettitt, "Importance nested sampling and the multinest algorithm," *The Open Journal of Astrophysics*, vol. 2, no. 1, Nov. 2019, ISSN: 2565-6120. DOI: 10.21105/astro.1306.2144.

[38] J. Buchner *et al.*, "X-ray spectral modelling of the agn obscuring region in the cdfs: Bayesian model selection and catalogue," *Astronomy and Astrophysics*, vol. 564, A125, Apr. 2014, ISSN: 1432-0746. DOI: 10.1051/0004-6361/201322971.

[39] E. Izaguirre, G. Krnjaic, P. Schuster, and N. Toro, "Analyzing the discovery potential for light dark matter," *Phys. Rev. Lett.*, vol. 115, p. 251 301, 25 Dec. 2015. DOI: 10.1103/PhysRevLett.115.251301.

[40] F. Kahlhoefer, K. Schmidt-Hoberg, T. Schwetz, and S. Vogl, "Implications of unitarity and gauge invariance for simplified dark matter models," *Journal of High Energy Physics*, vol. 2016, no. 2, Feb. 2016, ISSN: 1029-8479. DOI: 10.1007/jhep02(2016)016. [Online]. Available: http://dx.doi.org/10.1007/JHEP02(2016)016.

[41] J. Alexander *et al.*, *Dark sectors 2016 workshop: Community report*, 2016. arXiv: 1608.08632 [hep-ph].

[42] T. R. Gray, "How was Dark Matter Produced in the Early Universe? A Study of Fermionic Dark Matter with a Z-prime Portal," M.S. thesis, Ottawa U., 2020.

[43] J. D. Bjorken, R. Essig, P. Schuster, and N. Toro, "New fixed-target experiments to search for dark gauge forces," *Physical Review D*, vol. 80, no. 7, Oct. 2009, ISSN: 1550-2368. DOI: 10.1103/physrevd.80.075018.

[44] J. Alwall, M. Herquet, F. Maltoni, O. Mattelaer, and T. Stelzer, "Madgraph 5: Going beyond," *Journal of High Energy Physics*, vol. 2011, no. 6, Jun. 2011, ISSN: 1029-8479. DOI: 10.1007/jhep06(2011)128. [Online]. Available: http://dx.doi.org/10.1007/JHEP06(2011)128.

[45] C. Degrande, C. Duhr, B. Fuks, D. Grellscheid, O. Mattelaer, and T. Reiter, "Ufo – the universal feynrules output," *Computer Physics Communications*, vol. 183, no. 6, pp. 1201–1214, Jun. 2012, ISSN: 0010-4655. DOI: 10.1016/j.cpc.2012.01.022.

[46] C. Bini, *Data analysis in particle physics*, Feb. 2014. [Online]. Available: https://www.roma1.infn.it/~bini/StatEPP_new.pdf.

[47] S. Knapen, J. Kozaczuk, and T. Lin, "Dark matter-electron scattering in dielectrics," *Phys. Rev. D*, vol. 104, p. 015 031, 1 Jul. 2021. DOI: 10.1103/PhysRevD.104.015031.

[48] R. Essig, M. Fernández-Serra, J. Mardon, and I. Lorem, "Direct detection of sub-gev dark matter with semiconductor targets," *J. High Energ. Phys.*, vol. 2016, 46 2016. DOI: 10.1007/JHEP05(2016)046.

[49] S. Knapen, J. Kozaczuk, and T. Lin, "Migdal effect in semiconductors," *Phys. Rev. Lett.*, vol. 127, p. 081 805, 8 Aug. 2021. DOI: 10.1103/PhysRevLett.127.081805.

[50] M. J. Dolan, F. Kahlhoefer, and C. McCabe, "Directly detecting sub-gev dark matter with electrons from nuclear scattering," *Phys. Rev. Lett.*, vol. 121, p. 101 801, 10 Sep. 2018. DOI: 10.1103/PhysRevLett.121.101801.

[51] E. Aprile *et al.*, "Search for light dark matter interactions enhanced by the migdal effect or bremsstrahlung in xenon1t," *Physical Review Letters*, vol. 123, no. 24, Dec. 2019, ISSN: 1079-7114. DOI: 10.1103/physrevlett.123.241803.

[52] J. Enkovaara *et al.*, "Electronic structure calculations with gpaw: A real-space implementation of the projector augmented-wave method," *Journal of Physics: Condensed Matter*, vol. 22, no. 25, p. 253 202, Jun. 2010. DOI: 10.1088/0953-8984/22/25/253202. [Online]. Available: https://dx.doi.org/10.1088/0953-8984/22/25/253202.

[53] P. J. Brown, A. G. Fox, E. N. Maslen, M. A. O'Keefe, and B. T. M. Willis, "Intensity of diffracted intensities," in *International Tables for Crystallography*. International Union of Crystallography, Oct. 2006, pp. 554–595, ISBN: 9781402054082. DOI: 10.1107/97809553602060000600. [Online]. Available: http://dx.doi.org/10.1107/97809553602060000600.

[54] R. Essig, J. Pradler, M. Sholapurkar, and T.-T. Yu, "Relation between the migdal effect and dark matter-electron scattering in isolated atoms and semiconductors," *Physical Review Letters*, vol. 124, no. 2, Jan. 2020, ISSN: 1079-7114. DOI: 10.1103/physrevlett.124.021801.

[55] C. Arina, *Bayesian analysis of multiple direct detection experiments*, 2014. arXiv: 1310.5718 [hep-ph].

[56] W. "Press, S. Teukolsky, W. Vetterling, and B. Flannery, *Numerical Recipes 3rd Edition: The Art of Scientific Computing*. Cambridge University Press, 2007, pp. 110–124, 730–740, ISBN: 0070428077.

[57] D. S. Sivia and J. Skilling, *Data Analysis: A Bayesian Tutorial*, 2nd ed. Oxford University Press, 2006.

[58] C. Forssén and D. Phillips, *Learning from data: Assigning probabilities*, Sep. 2020. [Online]. Available: https://github.com/physics-chalmers/tif285.

[59] R. Trotta, "Bayes in the sky: Bayesian inference and model selection in cosmology," *Contemporary Physics*, vol. 49, no. 2, pp. 71–104, Mar. 2008, ISSN: 1366-5812. DOI: 10.1080/00107510802066753.

[60] J. S. Speagle, *A conceptual introduction to markov chain monte carlo methods*, 2020. arXiv: 1909.12313 [stat.OT].

[61] J. Skilling, "Nested Sampling," in *Bayesian Inference and Maximum Entropy Methods in Science and Engineering: 24th International Workshop on Bayesian Inference and Maximum Entropy Methods in Science and Engineering*, R. Fischer, R. Preuss, and U. V. Toussaint, Eds., ser. American Institute of Physics Conference Series, vol. 735, AIP, Nov. 2004, pp. 395–405. DOI: 10.1063/1.1835238.

[62] *e-Handbook of Statistical Methods*. NIST/SEMATECH. [Online]. Available: https://www.itl.nist.gov/div898/handbook/eda/section3/eda3674.htm.

A

Dark Bremsstrahlung Scattering Rate in the LDMX Experiment

In this appendix, we analytically derive the cross section for the production of a dark photon A' in a dark bremsstrahlung event (see figure 2.1). This proof is based on what is derived in [43] and the references therein.

The aim is to evaluate the following cross section

$$\frac{d\sigma(e(p)+Z(P_i)\to e(p')+A'(k)+Z(P_f))}{dE_{A'}d\cos(\theta_{A'})} \tag{A.1}$$

where $k=(E_{A'},\vec{k})$ is the four-momentum of the A', $\theta_{A'}$ is the angle of its momentum relative to the incoming electron with momentum $\vec{p}$ in the lab frame, $p=(E_0,\vec{p})$ and $p'=(E',\vec{p'})$ is the initial and final four-momenta of the electron, $P_i=(M_i,0)$ and P_f is the initial and final four-momenta of the nucleus with atomic number Z. We integrate over the momentum of the outgoing particles.

The incoming electron primarily interacts with an effective photon cloud, where transverse polarization interactions dominate [43]. As such, this process can be related to the cross section of real-photon scattering $e(p)\gamma(q)\to e(p')A'(k)$ with $q=P_i-P_f$

$$\frac{d\sigma(p+P_i\to p'+k+P_f)}{dE_{A'}d\cos(\theta_{A'})}=\frac{\alpha\chi}{\pi}\frac{E_0x\beta_{A'}}{1-x}\frac{d\sigma(p+q\to p'+k)}{d(p\cdot k)} \tag{A.2}$$

where $x\equiv E_{A'}/E_0$, $t\equiv -q^2$. Note the distinction between this t and the Mandelstam variable that we denote with t_2.

For a given k the virtuality t is at its minimum $t_{\min}$ when $\vec{q}$ is collinear with the three-vector $\vec{k}-\vec{p}$. The on-shell conditions state that ${p'}^2=(q+p+k)^2=m_e^2$ and $P_f^2=(P_i-q)^2=M_i^2$, and with the collinear geometry this gives the approximate solutions

$$q^0=\frac{|\vec{q}|^2}{2M_i}\approx 0,\quad |\vec{q}|=\left(\frac{U}{2E_0(1-x)}\right),\quad t_{\min}\approx\left(\frac{U}{2E_0(1-x)}\right)^2$$

where $U\equiv U(x,\theta_{A'})=E_0^2\theta_{A'}^2x+m_{A'}^2\frac{1-x}{x}+m_e^2x$. The kinematics are then given by

$$\begin{aligned}-\tilde{u}\equiv m_e^2-u_2&=2p\cdot k-m_{A'}^2=U\\ \tilde{s}\equiv s_2-m_e^2&=2p'\cdot k+m_{A'}^2=\frac{U}{1-x}\\ t_2\equiv(p-p')&=-\frac{Ux}{1-x}+m_{A'}^2\end{aligned}$$

where s_2, t_2 and u_2 are the Mandelstam variables for the $2 \to 2$ process. The cross section is now given by

$$\frac{d\sigma}{d(p \cdot k)} = 2\frac{d\sigma}{dt_2} \approx \frac{1}{8\pi(s_2 - m_e^2)^2}|\mathcal{M}|^2 = \frac{4\pi\alpha^2\varepsilon^2}{\tilde{s}^2}\left(\frac{\tilde{s}}{-\tilde{u}} + \frac{-\tilde{u}}{\tilde{s}} + \frac{2m_{A'}^2 t_2}{-\tilde{u}\tilde{s}}\right). \tag{A.3}$$

Finally we see that the Weizsäcker-Williams approximation to the cross section in Equation (A.1) is given by

$$\begin{aligned}\frac{1}{E_0^2 x}\frac{d\sigma_{3\to 2}}{dx d\cos(\theta_{A'})} =& 8\alpha^3\varepsilon^2\chi\sqrt{1 - \frac{m_{A'}^2}{E_0^2}} \\ &\times \left(\frac{1 - x + \frac{x^2}{2}}{U^2} + \frac{(1-x)^2 m_{A'}^2}{U^4}\left(m_{A'}^2 - \frac{Ux}{1-x}\right)\right)\end{aligned} \tag{A.4}$$

where χ is an effective photon flux that is integrated over the total center of mass energy in the collision. For a general electric form factor $G_2(t)$ this is given by

$$\chi \equiv \int_{t_{\min}}^{t_{\max}} \frac{t - t_{\min}}{t^2} G_2(t) dt. \tag{A.5}$$

B

Electron Scattering Rate in a Direct Detection Experiment

Here we derive the formula for the electron scatter rate presented in Equation (3.4). This is the underlying equation utilized by electron scattering simulation in DarkELF [21] and as such it is central to this project. The proof shown here follows the steps taken in [47].

The first part of this proof is to derive the structure factor $S(\omega, \mathbf{k})$ as a function of the dielectric function $\epsilon(\omega, \mathbf{k})$.

The energy loss function (ELF) describing the rate of energy and momentum loss for a particle traveling through a given material, can be defined in terms of the dielectric function as

$$\text{ELF} = \text{Im}\left[\frac{-1}{\epsilon(\omega, \mathbf{k})}\right]. \tag{B.1}$$

Here $\epsilon(\omega, \mathbf{k})$ encapsulates the dielectric response of the material for incoming energies ω that are above the band gap.

The dark photon can be treated as an external source that couples to the electron number density $n(\mathbf{r},t)$ of the material. We can use linear response theory to treat the incoming particle as a perturbation of $n(\mathbf{r},t)$. This allows us to determine the susceptibility as

$$\chi(\omega, \mathbf{k}) = -\frac{i}{V}\int_0^\infty dt e^{i\omega t}\langle[n_{\mathbf{k}}(t), n_{-\mathbf{k}}(0)]\rangle, \tag{B.2}$$

which is the definition of the Fourier transform of the leading order response of an electric system. The susceptibility $\chi(\omega, \mathbf{k})$ as defined here is intimately related to the dielectric response $\epsilon(\omega, \mathbf{k})$ as

$$\frac{1}{\epsilon(\omega, \mathbf{k})} = 1 + \frac{4\pi\alpha_{em}}{k^2}\chi(\omega, \mathbf{k}). \tag{B.3}$$

Furthermore, the fluctuation-dissipation theorem can be used to relate the susceptibility $\chi(\omega, \mathbf{k})$ to the dynamical structure factor $S(\omega, \mathbf{k})$ as

$$\text{Im}\chi(\omega, \mathbf{k}) = -\frac{1}{2}(1 - e^{-\beta\omega})S(\omega, \mathbf{k}). \tag{B.4}$$

The dynamical structure factor $S(\omega, \mathbf{k})$ parametrizes the rate at which excitations are emitted or absorbed and is defined as

$$S(\omega, \mathbf{k}) = \frac{2\pi}{V}\sum_{i,f}\frac{e^{-\beta E_i}}{Z}|\langle f|\, n_{-\mathbf{k}}\, |i\rangle|^2\delta(\omega + E_i - E_f) \tag{B.5}$$

where $\beta = \frac{1}{k_B T}$ and Z is the partition function. Equation (B.3) relates $\epsilon(\omega, \mathbf{k})$ to $\chi(\omega, \mathbf{k})$ and Equation (B.4) relates $\chi(\omega, \mathbf{k})$ to $S(\omega, \mathbf{k})$. Putting these together, we can express $S(\omega, \mathbf{k})$ as a function of $\epsilon(\omega, \mathbf{k})$ as

$$S(\omega, \mathbf{k}) = -2\frac{1}{(1 - e^{-\beta\omega})}\text{Im}\chi(\omega, \mathbf{k}) = -2\frac{1}{(1 - e^{-\beta\omega})}\text{Im}(\frac{1}{\epsilon(\omega, \mathbf{k})} - 1)\frac{k^2}{4\pi\alpha_{em}}$$

and so we conclude that

$$S(\omega, \mathbf{k}) = \frac{k^2}{2\pi\alpha_{em}}\frac{1}{1 - e^{-\beta\omega}}\text{Im}(\frac{-1}{\epsilon(\omega, \mathbf{k})}). \tag{B.6}$$

The second part of the proof will now be to derive the DM-electron scattering rate R using this relation. Remember that we are using a mediator dark photon in our model, so the interaction will be given by the coupling between the DM and the DP g_χ and the coupling between the DP and the electron $g_e = \epsilon q$. With this in mind, the coupling between the electron density perturbation $n_\mathbf{k}$ and the DM potential is given by the Hamiltonian

$$H_{ext} = \int \frac{d^3\mathbf{k}}{(2\pi)^3} n_\mathbf{k} \times \left(\frac{g_\chi g_e e^{i\mathbf{k}\cdot\mathbf{x}}}{k^2 + m_{A'}^2}\right). \tag{B.7}$$

Note that we consider the external Hamiltonian here as it represents the unscreened potential. A screened potential would have included a factor $\frac{1}{\epsilon(\omega,\mathbf{k})}$ in the propagator, but this is instead included in the dynamical structure factor $S(\omega, \mathbf{k})$. It is completely equivalent to instead include the screening factor in the propagator. With this remark aside, we can now evaluate the Hamiltonian (B.7) between an initial and final DM state by using the matrix element

$$\mathcal{M} = \frac{g_\chi g_e}{V(k^2 + m_{A'}^2)} \langle f| n_{-\mathbf{k}} |i\rangle \delta_{\mathbf{p}_i - \mathbf{p}_f, \mathbf{k}}. \tag{B.8}$$

Applying Fermi's golden rule to this process, summed over initial states $|i\rangle$ weighted with $\frac{e^{-\beta E_i}}{Z}$ and summed over final states $\langle f|$, we arrive at the DM scattering rate

$$R = \frac{1}{\rho_T}\frac{\rho_\chi}{m_\chi}\frac{\pi\bar{\sigma}_e}{\mu_{\chi e}^2}\int d^3v f_\chi(v)\int \frac{d^3\mathbf{k}}{(2\pi)^3}k^2\int\frac{d\omega}{2\pi}\times\delta\left(\omega + \frac{k^2}{2m_\chi} - \mathbf{k}\cdot\mathbf{v}\right)|F_{DM}(k)|^2 S(\omega, \mathbf{k}). \tag{B.9}$$

Plugging in Equation (B.6) for $S(\omega, \mathbf{k})$ we arrive at the final expression for the DM-electron scattering rate in units of the number of counts per exposure

$$\begin{aligned} R =& \frac{1}{\rho_T}\frac{\rho_\chi}{m_\chi}\frac{\bar{\sigma}_e}{\mu_{\chi e}^2}\frac{\pi}{\alpha}\int d^3v f_\chi(v)\int\frac{d^3\mathbf{k}}{(2\pi)^3}k^2|F_{DM}(k)|^2\int\frac{d\omega}{2\pi} \\ &\times\frac{1}{1 - e^{-\beta\omega}}\text{Im}\left[\frac{-1}{\epsilon(\omega,\mathbf{k})}\right]\delta\left(\omega + \frac{k^2}{2m_\chi} - \mathbf{k}\cdot\mathbf{v}\right). \end{aligned} \tag{B.10}$$

C

Extra Figures

C.1 Validation Results with a Germanium Direct Detection Experiment

Figure C.1 shows the result of an identical analysis to that of Figure 4.3, with the exception that the DD target material used here is germanium instead of silicon. We see that a germanium based experiment requires slightly more exposure to validate the LDMX signal for the m_χ values considered here, although the difference is relatively small.

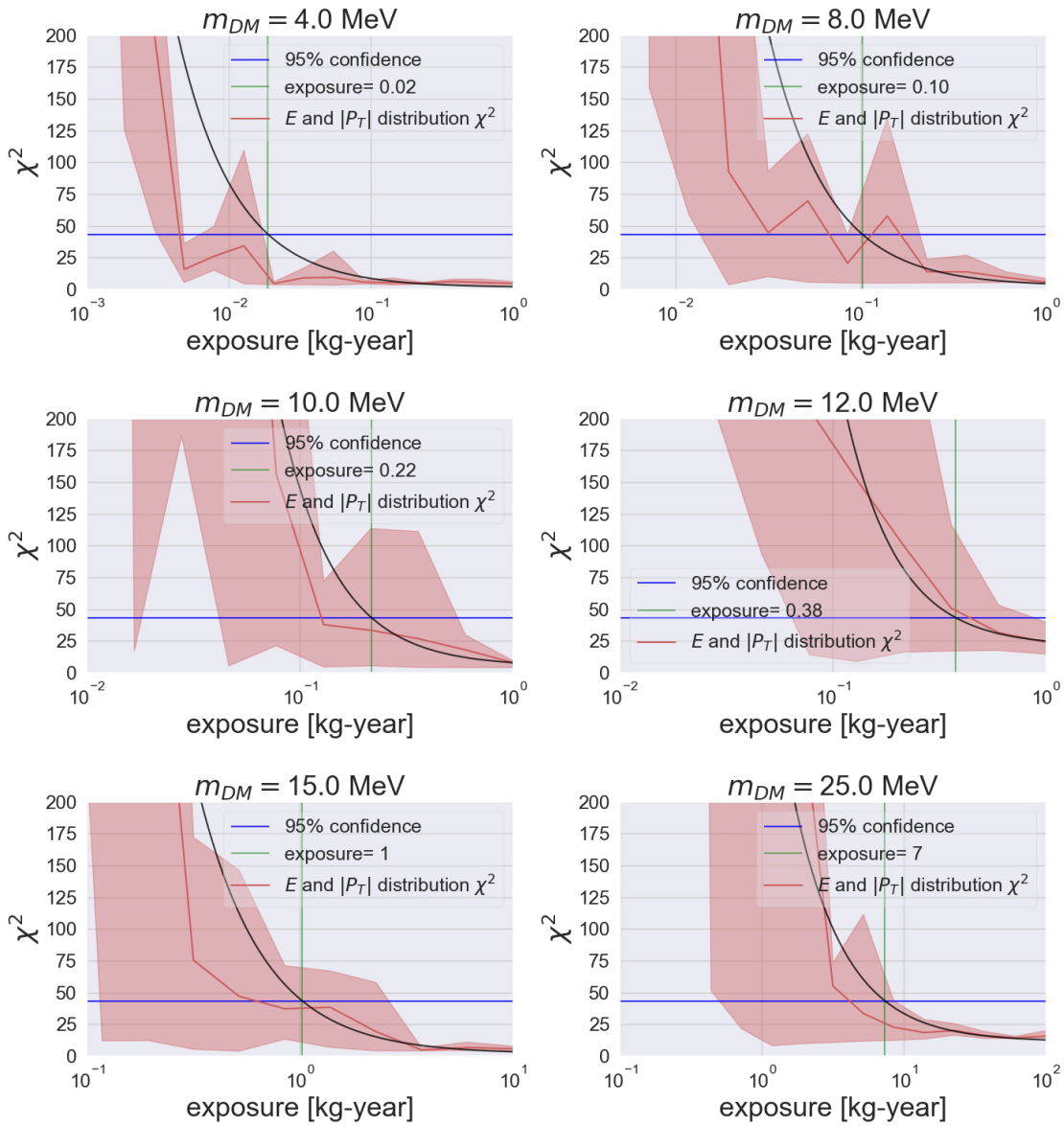

Figure C.1: The result of a χ^2 test applied to the E and $|P_T|$ distributions of LDMX and the direct detection prediction for varying true dark matter mass. On the x-axis is the exposure of the direct detection experiment. A stable χ^2 value below 95% confidence is considered a validation of the LDMX signal. The black curve in each figure shows the fit of an exponential decay function to the mean of the results. When this fit falls below 95% confidence, we mark out the exposure. Compared to figure 4.2 the DD target material used here is germanium.

Division of Subatomic, High Energy and Plasma Physics
Chalmers University of technology
Gothenburg, Sweden
www.chalmers.se

CHALMERS
UNIVERSITY OF TECHNOLOGY